FLOW PAST A SPHERE AND A PROLATE SPHEROID AT LOW REYNOLDS

NUMBERS

A Thesis

by

YOUFENG ZHANG

Submitted to the Office of Graduate and Professional Studies of
Texas A&M University
in partial fulfillment of the requirements for the degree of

MASTER OF SCIENCE

Chair of Committee,   Robert Handler
Committee Members,   Devesh Ranjan
                                   Hamnching Chen
Head of Department,   Andreas A. Polycarpou

December 2013

Major Subject: Mechanical Engineering

ABSTRACT

The present work carries out numerical simulations of viscous incompressible flow past a sphere or a spheroid at low Reynolds numbers. When the flow passes a sphere or a spheroid, the flow will have its motion changed because of the shear stress from the surface of the object. This change of motion also differs at different Reynolds numbers based on the geometry of the sphere or spheroid.

Many fluids researchers have conducted experiments to investigate the variations of the flow past a sphere at low Reynolds numbers. But the research on flow past a spheroid mainly focuses on cases at high Reynolds numbers ($Re>10^5$). Up to date, numerical study on flow past a spheroid at low and intermediate Reynolds numbers (<1000) has not been done thoroughly.

The first part of this work is to investigate variations of the flow past a sphere occurring with increasing Reynolds number up to 400. The code used in this thesis is OpenFOAM which is an open source package providing a solver based on the Finite Volume Method. To verify the accuracy of the simulations by the code, results for velocity, vorticity and drag coefficient at very low Reynolds number (Re<0.1) are compared with exact solutions by Stokes Law. Then variations of the flow pattern are displayed up to Reynolds number 400. Some characteristics such as the drag coefficient, wake length and wake angle are recorded for contrast with data in publications. The wake length and separation angle both show logarithmic relationship with the Reynolds

number. Flow patterns such as streamline around the sphere and periodic shedding are also discussed on the ground of previous knowledge.

The second part will investigate the flow past a prolate spheroid. Discussion on this topic is developed in the regime of low Reynolds number (Re<1000). The present work investigates cases at very low Reynolds numbers (Re<0.1) and compares the results with exact solutions predicted by previous researchers. For higher Reynolds numbers, present work mainly focuses on studying variations of the drag coefficient with the Reynolds number and aspect ratio. The simulation shows that a spheroid has larger drag coefficient than a sphere at lower Reynolds numbers and then tends to be the smaller one for higher Reynolds numbers.

DEDICATION

To God for his love.

To parents for their love and tolerance.

To Dr. Handler for his patient teaching. What he has taught me is knowledge in

not only fluid mechanics but also how to behave properly in United States. His

enthusiasm for research set up an example for me which is beneficial forever.

ACKNOWLEDGEMENTS

I would like to thank my committee chair, Dr. Handler, and my committee members, Dr. Chen, and Dr. Ranjan, for their guidance and support throughout the course of this research.

I want to give my additional appreciation to Dr. Handler who is both great as a human being and a scientist. From the discussions with him, I benefit a lot. His passion and curiosity to explore unknown and sensitivity to science impress and educate me deeply.

Also I want to thank my group members, Qi Shao and Qi Zhang, for their assistance in running OpenFOAM and the supercomputer. Qi Shao, my group member, has been working with me on CFD and always very helpful with my work.

Thanks also go to my friends and colleagues and the department faculty and staff for making my time at Texas A&M University a great experience.

Finally, thanks to my mother and father for their encouragement and to my girlfriend for her patience and love.

NOMENCLATURE

a	Major Axis Length of the Spheroid
b	Minor Axis Length of the Spheroid
c	Half Focal Length of the Spheroid
C_D	Drag Coefficient
C_P	Pressure Coefficient
D	Drag Force
$\mathbf{D}_{sphere}$	Drag Force on a Sphere
e	Eccentricity of the Spheroid
$\mathbf{e_x}$	Unit Vector in *x* Axis
$\mathbf{e_y}$	Unit Vector in *y* Axis
$\mathbf{e_z}$	Unit Vector in *z* Axis
$\vec{g}$	Gravitational Acceleration
L	Characteristic Length for Reynolds Number
p	Pressure
q	Velocity at the Infinity
r	Radius of the Sphere or Spherical Coordinate
Re	Reynolds Number
R_a	Reynolds Number Based on *a*
R_b	Reynolds Number Based on *b*
s	Wake Length

t	Time
U	Velocity Magnitude at the Inlet
U_r	Velocity along the Radial Direction
U_θ	Velocity along the Azimuth Angle Direction
U_φ	Velocity along the Zenith Angle Direction
u	Velocity along x Axis
$\vec{V}$	Velocity Vector
v	Velocity along y Axis
w	Velocity along z Axis
υ	Kinematic Viscosity
ϕ	Potential Function
Ψ	Stream Function
μ	Dynamic Viscosity
ω	Vorticity
θ	Azimuth Angle in the Spherical Coordinate
φ	Zenith angle in the Spherical Coordinate

TABLE OF CONTENTS

LIST OF FIGURES

LIST OF TABLES

1. INTRODUCTION AND BACKGROUND

1.1 Literature review

It is known that the Stokes' Law provides an approximated exact solution at sufficiently low Reynolds number for flow past a sphere. Lamb (1934) discussed detailed solutions for this type of flow in his book *Hydrodynamics* [1].

There are many archived publications focus on investigations of the behavior of the flow past a sphere. Taneda (1956) photographically investigated flow past a sphere at Reynolds numbers from 5 to 300 [2]. He found the critical Reynolds number (Re=24) when a double-ring looking wake after the sphere begins to show up. He also investigated the variations of size and position of the wake with respect to the Reynolds number. According to his test data, the wake length increases linearly with the logarithm of the Reynolds number. At a Reynolds number of about 130, he observed that the flow began to oscillate.

Magarvey and Bishop (1961) photographically depicted wake configurations in a liquid due to the passage of a falling immiscible liquid drop (Carbon Tetrachloride) corresponding to Reynolds numbers between 10 and 2500 [3]. Although it is a liquid-liquid system, both the pattern of the wake and the wake length data showed good correlation with that by Taneda. The paper reported that the transition from one wake to a double-ring wake behind the sphere occurs at a Reynolds number somewhat less than 20. At Reynolds number 210, the authors observed a transition of the flow pattern from a symmetrical and single thread to an asymmetrical and double thread. Then at the

Reynolds number between 270 and 290, this double thread oscillated periodically. After Reynolds number 290 up to 400, they reported a double row of vortex rings after the drop. They were the first to find a linear relationship between the Strouhal number and Reynolds number for this range, which was reported to occur at Reynolds number between 290 and 700.

Rimon and Cheng (1969) performed a numerical work for flow past a sphere at Reynolds number from 1 to 1000 [4]. Their work was based on a second order finite difference approximation both in time (Dufort- Frankel) and space. They compared their results for the wake length and wake angle with Taneda's data and claimed that a recirculating eddy even existed at Reynolds number of 10.

Roos and Willmarth (1971) presented specific experimental results of the drag coefficient on a sphere for Reynolds number ranging from 5.33 to 118300 [5]. These results contain test data at many Reynolds numbers and are frequently cited in subsequent publications.

Nakamura (1976) used dye for visualization to examine the wake configurations after a sphere falls in water at terminal velocity [6]. He focused on the investigation of the wake shape, and more specifically, the separation angle of the wake. The results coincide well with Taneda's work at Reynolds numbers larger than 30, but show significant discrepancies at Reynolds numbers lower than 30. He also found a critical Reynolds number (Re=7.3) at which the wake began to develop double-ring eddies and a critical Reynolds number (Re=190), where he found a double thread wake.

Fornberg(1988) reported situational results for wake length and drag coefficients for Reynolds numbers from 100 up to 2000 [7]. His results show agreement with Taneda(1965) and Roos & Willmarth(1971) at Reynolds number up to 200.

Sakamoto and Haniu(1999) investigated the shedding frequency after Reynolds number 300 and found that the variations of the shedding can be classified by four regions [8]. Later they also (1995) attempted to explain the formation mechanism of the periodic shedding behind a sphere passed by a uniform shear flow at Reynolds numbers ranging from 200 to 3000 [9]. From the experiment, they observed a lower critical Reynolds number for vortex shedding and a higher Strouhal number for the shedding than that for a uniform incident flow. They also determined the variations of the Strouhal number with Reynolds number up to 3000.

Johnson and Patel (1999) used a four-stage Runge-Kutta integration method to numerically simulate flow past a sphere up to Reynolds numbers of 300. They identified three stages of the flow by means of the flow pattern: steady axisymmetric flow, steady non-axisymmetric flow and unsteady flow [10].

Tomboulides and Orszag (2000) are the first to present simulations of viscous incompressible flow past a sphere by using Direct Numerical Simulation (DNS) based on spectral methods [11]. The authors investigated characteristics of the flow for Reynolds numbers from 25 up to 1000. Their results include wake lengths, separation angles, pressure coefficients, vorticity patterns, and Strouhal numbers. They compared these results with previous data and showed good correlation.

There are generally less publications on flow past spheroid than sphere. Bus as early as in 1910, Ossen proposed linearized equations of motion for an incompressible viscous flow past a rigid sphere when the Reynolds number is fairly small [12]. Oseen also gave an analytic solution for the drag force as a function of the aspect ratio and the Reynolds number in his book [13]. A fitting curve formula for the drag coefficient with respect to the Reynolds number was provided by [14].

Other researchers such as Aoi (1955) [15] and Breach (1961) [16] derived exact solutions of drag coefficients for flow past oblate and prolate spheroids at low Reynolds number.

Rimon and Lugt (1969) numerically studied flow past oblate spheroids at Reynolds numbers of 10 and 100 [17]. They compared pressure and vorticity around the sphere at different aspect ratios and found the larger aspect ratio of the oblate spheroid is, the higher vorticity and pressure around it are, so as the drag coefficient on the spheroid is.

Masliyah and Epstein (1970) studied the steady incompressible flow past oblate and prolate spheroids for Reynolds number up to 100 [18]. The aspect ratios they used were 5, 2 and 10/9 together for prolate spheroids and 0.2, 0.5, 0.9 for oblate spheroids, together with 1 representing the case of a sphere. They presented variations of pressure coefficients, drag coefficients and wake lengths with the Reynolds number at different aspectios.

Chwang and Wu (1976) analyzed a uniform flow past a prolate spheroid at low Reynolds number [19]. By changing the slenderness ratio, they obtained results for drag

4

coefficient and compared their work with predictions by theories of Oberbeck [12] and Oseen[13] at low Reynolds numbers.

1.2 Research methodology

The simulations are performed by using OpenFOAM, an open source CFD program developed by using C++. The solver for present simulations is IcoFOAM which applies the Finite Volume Method with a transient solver based on the PISO (Pressure Implicit Splitting of Operators) algorithm for incompressible flow. The present work utilizes approximated exact solutions by Stokes [1] for flow past a sphere or a spheroid at low Reynolds numbers (Re<0.1) to benchmark the simulation results obtained by OpenFOAM. For higher Reynolds numbers (Re>1), present work studied variation of the flow pattern including the streamline profile and the wake length, as well as the drag coefficient. These numerical results are compared with published results by Taneda [2], Roos and Willmarth [4] and Orszag [10]. The second part of this work discusses simulations for flow past a spheroid at variable Reynolds number and spheroid aspect ratios. Simulations for drag coefficient at very low Reynolds numbers (Re<0.1) are compared with published exact solutions by Oseen[13]. Drag coefficients for spheroids with several aspect ratios at higher Reynolds number are also investigated and found to behave different relations with the results for a sphere.

2. NUMERICAL SIMULATION AT VERY LOW REYNOLDS NUMBER

2.1 Basic theory for Stokes Flow

The Navier-Stokes Equation for a Newtonian incompressible flow reads

$$\frac{\partial \vec{V}}{\partial t} + \vec{V} \bullet \nabla \vec{V} = -\frac{\nabla p}{\rho} + \nu \nabla^2 \vec{V} + \vec{g} \quad . \tag{2.1}$$

The flow also satisfies the continuity equation:

$$\nabla \bullet \vec{V} = 0. \tag{2.2}$$

Neglect gravity and assume steady-state, then the Navier-Stokes equation becomes

$$-\frac{\nabla p}{\rho} + \nu \nabla^2 \vec{V} = 0. \tag{2.3}$$

From definition of the Reynolds number,

$$\text{Re} = \frac{\overline{|\vec{V}|}L}{\nu} \quad . \tag{2.4.1}$$

We know that for very low Reynolds number, Re<<1, the inertia effects are very small compared with viscous effects.   Such a flow is named Stokes flow named after the famous mathematician George Gabriel Stokes, or creeping flow. One of the most classical cases in low Reynolds-number hydrodynamics is the Stokes solution for steady flow past a sphere, which is refereed as the Stokes Law in this thesis. Applications of the Stokes law range from electron charges to the physics of aerosols. For better understanding the theory, this work rederives the solution as following.
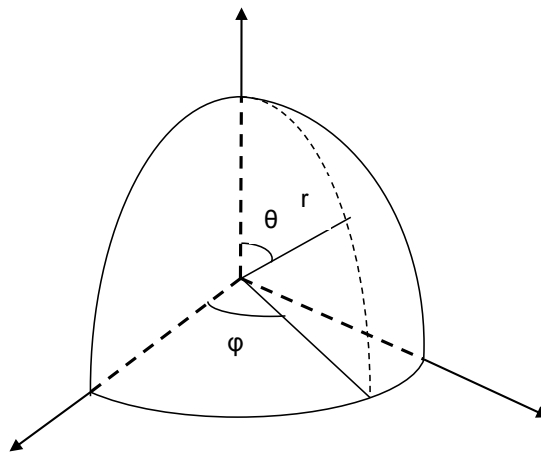
Figure 1 Nomenclature of flow past a sphere

Figure 2 Spherical coordinate system of the flow

The continuity equations gives

$$\nabla \cdot \vec{V} = 0 . \tag{2.4.2}$$

With inertia effects neglected the Naiver-Stokes equation becomes

$$-\frac{\nabla p}{\rho} + \nu \nabla^2 \vec{V} = 0 . \tag{2.4.3}$$

Conversion from the Cartesian coordinate system to the spherical coordinate system gives

$$\begin{cases} x = r\cos\varphi\sin\theta \\ y = r\sin\varphi\sin\theta \\ z = r\cos\theta \end{cases}.$$ (2.5.1)

And velocities converted to the spherical coordinate become

$$\begin{cases} U_r = \dfrac{\partial\phi}{\partial x}\dfrac{\partial x}{\partial r} + \dfrac{\partial\phi}{\partial y}\dfrac{\partial y}{\partial r} + \dfrac{\partial\phi}{\partial z}\dfrac{\partial z}{\partial r} = U\cos\varphi\sin\theta + V\sin\varphi\sin\theta + W\cos\theta \\[2mm] U_\theta = \dfrac{\partial\phi}{\partial x}\dfrac{\partial x}{r\partial\theta} + \dfrac{\partial\phi}{\partial y}\dfrac{\partial y}{r\partial\theta} + \dfrac{\partial\phi}{\partial z}\dfrac{\partial z}{r\partial\theta} = U\cos\varphi\cos\theta + V\sin\varphi\cos\theta - W\sin\theta \\[2mm] U_\varphi = \dfrac{\partial\phi}{\partial x}\dfrac{\partial x}{r\partial\varphi} + \dfrac{\partial\phi}{\partial y}\dfrac{\partial y}{r\partial\varphi} + \dfrac{\partial\phi}{\partial z}\dfrac{\partial z}{r\partial\varphi} = -U\sin\varphi\sin\theta + V\cos\varphi\sin\theta \end{cases}$$ (2.5.2)

For very slow flow, the flow is laminar and does not have rotation about z-axis,

$$U_\varphi = 0.$$ (2.6)

The continuity equation in the spherical coordinate gives

$$\frac{1}{r^2}\frac{\partial}{r}(r^2 U_r) + \frac{1}{r\sin\theta}\frac{\partial}{\partial\theta}(U_\theta\sin\theta) = 0.$$ (2.7)

As r goes to infinity,

$$\begin{cases} U_\theta = -U\sin\theta \\ U_r = U\cos\theta \end{cases}.$$ (2.8)

In the spherical coordinate, the stream function ψ is defined as:

$$\begin{aligned} U_r &= \frac{1}{r^2\sin\theta}\frac{\partial\psi}{\partial\theta} \\ U_\theta &= -\frac{1}{r\sin\theta}\frac{\partial\psi}{\partial r} \end{aligned}.$$ (2.9)

The stream function can be obtained by integration:

$$\psi = \frac{W}{2} r^2 \sin^2 \theta , \ r = \infty , \tag{2.10.1}$$

$$\nabla \times (\nabla \times \vec{V}) = \nabla (\nabla \bullet \vec{V}) - \nabla^2 \vec{V} . \tag{2.10.2}$$

Because of the continuity condition, $\nabla \bullet \vec{V} = 0$, we can have

$$\nabla \times (\nabla \times \vec{V}) = -\nabla^2 \vec{V} , \tag{2.11}$$

where $\vec{\zeta} = \nabla \times \vec{V}$ is the vorticity.

Take curl of the N-S Equation,

$$-\frac{\nabla \times \nabla p}{\rho} + \nu \nabla \times (\nabla^2 \vec{V}) = 0 . \tag{2.12}$$

$\nabla \times \nabla p = 0$ because p is a scalar, thus,

$$-\nabla \times \nabla^2 \vec{V} = \nabla \times \nabla \times (\nabla \times \vec{V}) = 0 . \tag{2.13}$$

Since $\vec{V} = \nabla \times \left(\dfrac{\psi \vec{e}_\varphi}{r \sin \theta} \right)$, we have

$$\nabla \times \nabla \times \nabla \times \left(\frac{\psi \vec{e}_\varphi}{r \sin \theta} \right) = 0 , \tag{2.14}$$

$$\left(\frac{\partial^2}{\partial r^2} + \frac{\sin \theta}{r^2} \frac{\partial}{\partial \theta} \left(\frac{1}{\sin \theta} \frac{\partial}{\partial \theta} \right) \right)^2 \psi = 0 . \tag{2.15}$$

With boundary conditions:

$$u_r = u_\theta = 0 \ \text{at } r = a, \tag{2.16}$$

$$\psi = \frac{U}{2} r^2 \sin^2 \theta \ \text{at } r \to \infty , \tag{2.17}$$

the stream function can be obtained as:

$$\psi = \frac{U}{2}\left[r^2 + \frac{a^3}{2r} - \frac{3ar}{2} \right]\sin^2\theta .$$

(2.18)

Correspondingly, the velocities along r and θ directions are:

$$u_r = U\cos\theta\left[1 + \frac{a^3}{2r^3} - \frac{3a}{2r} \right]$$

$$u_\theta = -U\sin\theta\left[1 - \frac{a^3}{4r^3} - \frac{3a}{4r} \right]$$

(2.19)

Meanwhile, other properties of the flow are as following.

Vorticity, $\vec{\zeta} = -\frac{3}{2}Ua\frac{\sin\theta}{r^2}\vec{e}_\phi$.

(2.20)

Pressure. From the N-S equation, $\frac{\partial p}{\partial r} = \frac{\mu Ua}{r^3}\cos\theta$. Integrating both sides with

respect to r yields $p = p_\infty - \frac{3}{2}\frac{\mu Ua}{r^3}\cos\theta$.

(2.21)

The following part of this chapter would compare simulation results from exact

solutions for velocity, vorticity and pressure.

2.2 Comparison of simulation with theoretical predictions

2.2.1 Velocity

At $\theta = 0$ and π , we can have sinθ=0, $\cos\theta = 1$ and -1 respectively. In that case,

the velocity is equal to radial velocity, $u = u_r$. Figure 3 and

Figure 4 shows simulation results for streamlines and velocity magnitude at

Reynolds number of 0.01. At such a low Reynolds number, the flow is symmetrical

about the parallel centerline and shows diffusive profile in the velocity field.
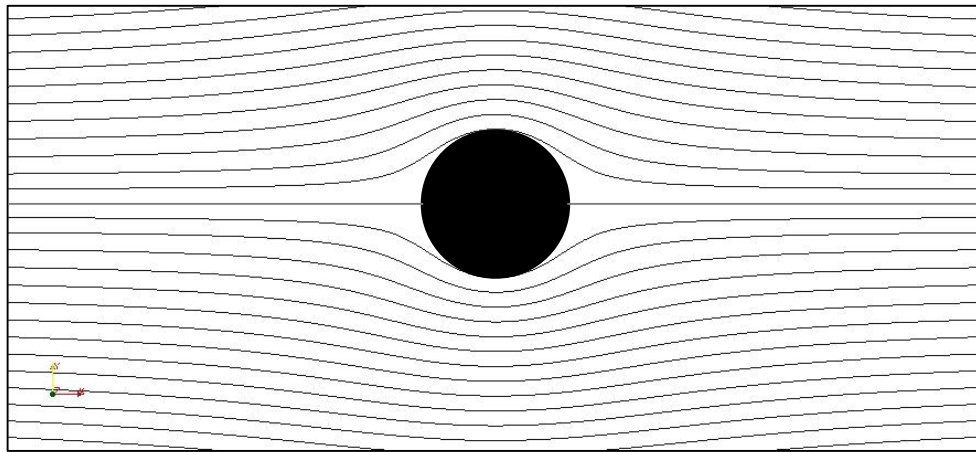
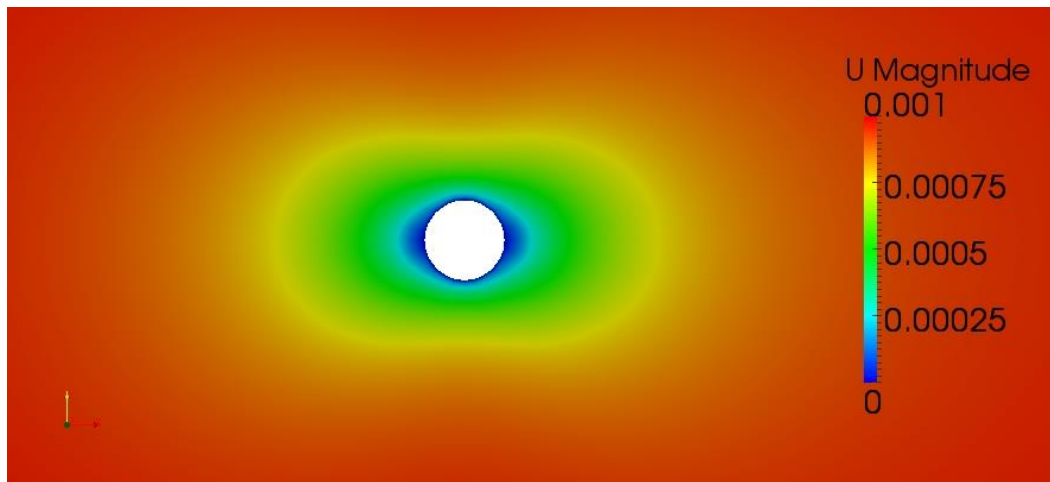Figure 3 Streamlines of flow past sphere at low Reynolds number (Re=0.01)

Figure 4 Velocity magnitude contour for flow past sphere at Re=0.01

Figure 5, Figure 6 and Figure 7 demonstrate velocity magnitude versus x

coordinate computed by present work and predictions by the Stokes Law, given in the

Equation (2.16). The three cases apply different domains, with box length increasing

from 20a to 40a. As can be seen from the three figures, the two results by OpenFOAM and the Stokes Law show better agreement for larger domain. The difference for the two results is caused by the fact that OpenFOAM sets fixed inlet boundary conditions at the inlet and outlet and begins computation from there while the StokesLaw begins its calculation from the center of the sphere. It is not difficult to foresee that the difference will be negligibly small when the domain is sufficiently large.
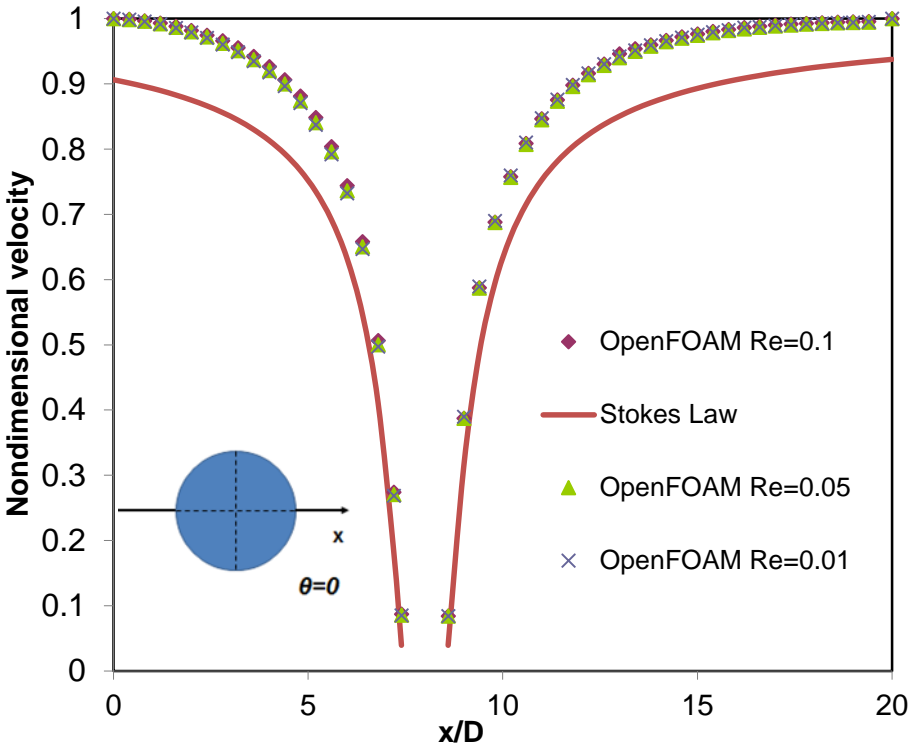

Figure 5 Velocity along θ=0 for L=20D (Re=0.01)

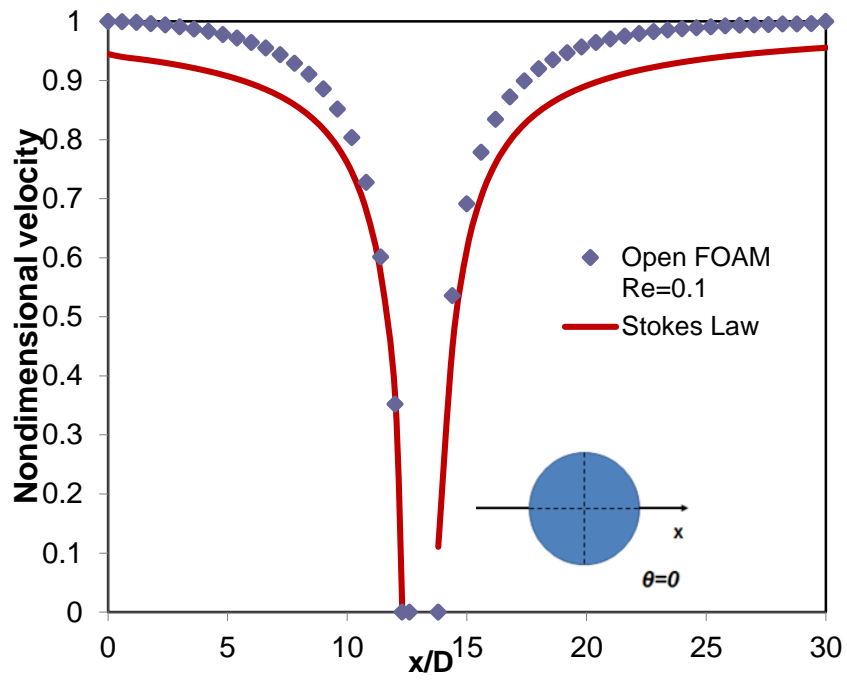Figure 6 Velocity along θ=0 for L=30D (Re=0.01)

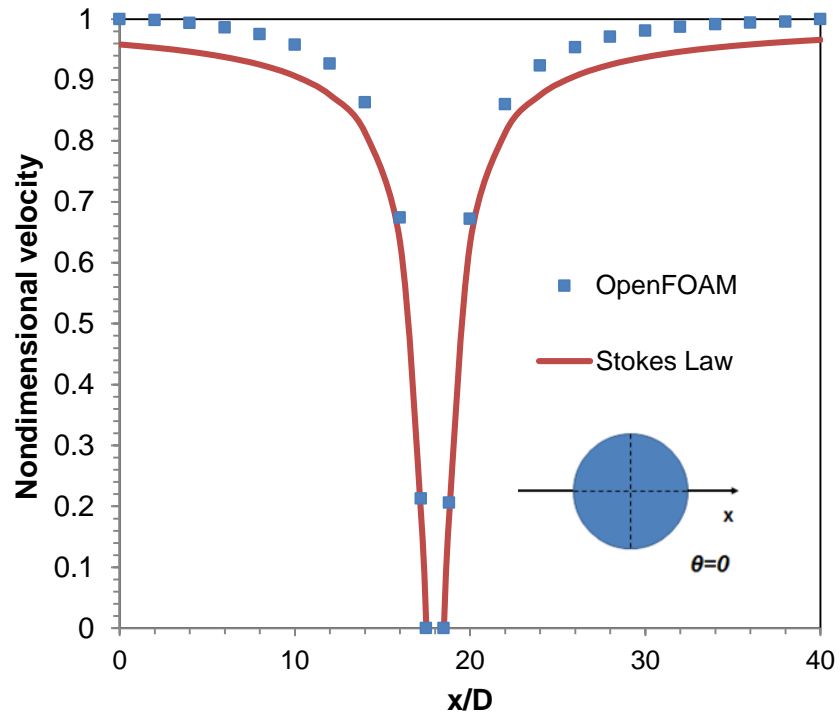Figure 7 Velocity along θ=0 for L=40D (Re=0.01)

13

2.2.2 Vorticity

Equation (2.22) gives the expression for the vorticity:

$$\vec{\zeta} = -\frac{3}{2}Ua\frac{\sin\theta}{r^2}\vec{e}_\phi = --\frac{3}{2}\frac{Uay}{(x^2+y^2)^{\frac{3}{2}}}\vec{e}_\phi.$$

(2.22)

Equation (2.19) transforms the solution from the cylindrical coordinate system into the Cartesian coordinate system. For convenience of comparison, here this thesis only takes the results along the line $x=4a$. Figure 8 shows the vorticity plotted in contour and Figure 9 to Figure 11 display predicted vorticity magnitude along the line at increasing domains. Figure 9 reveals that there is little relevance between situational results and magnitude of the Reynolds number provided that the Reynolds number is sufficiently small, since here we obtain almost the same results for Re=0.01 and Re=0.1. The three pictures from Figure 9 to Figure 11 denote that the larger the domain is the better the situational results coincide with the curves plotted from the Stokes law. When the height of the box is 40 diameters of the sphere, the two results agree with each other very well, see the Figure 11.
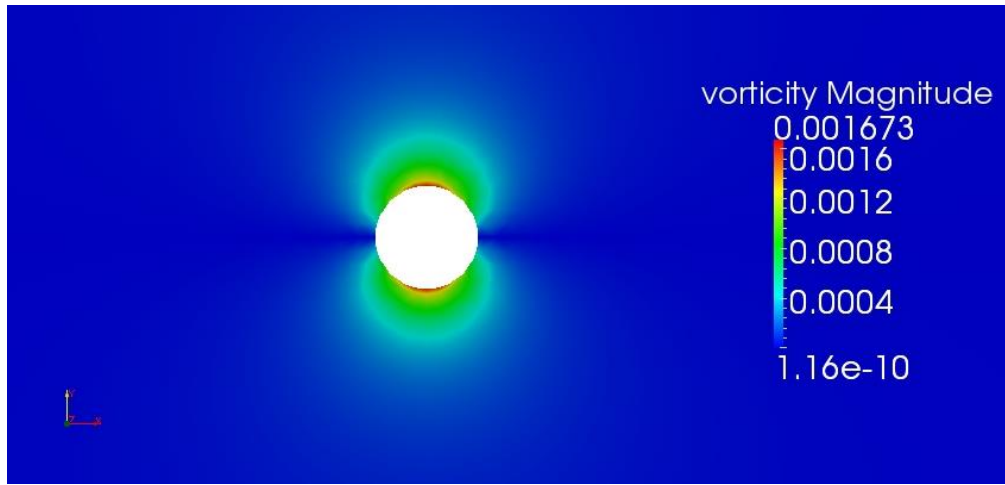
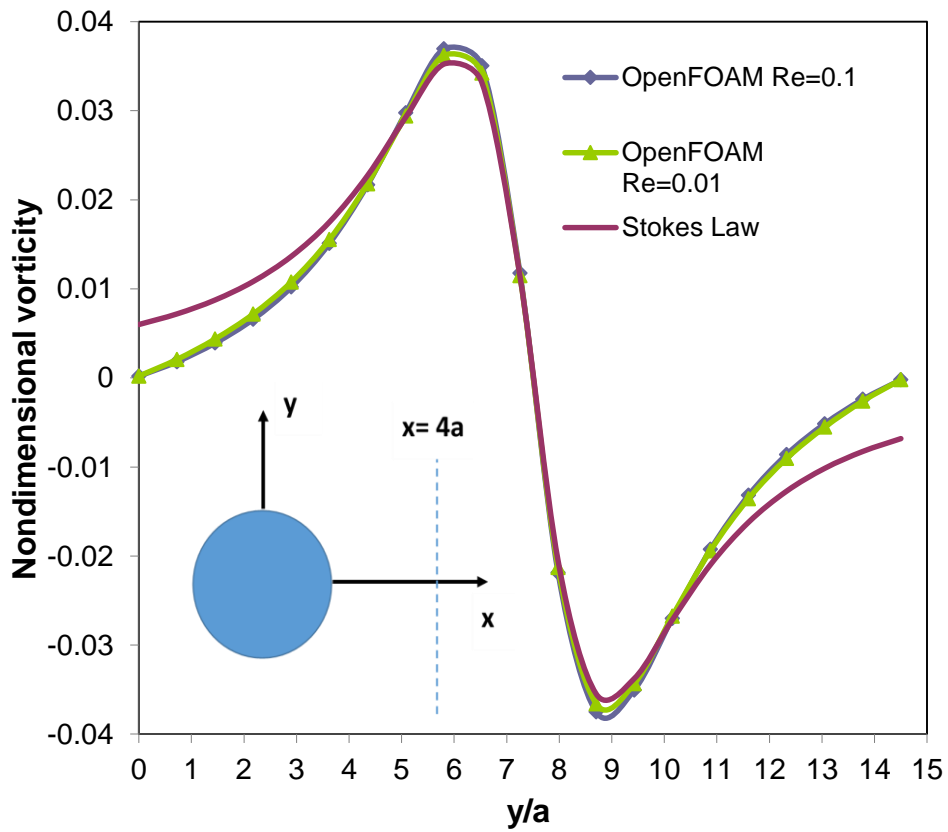Figure 8 Vorticity contour for flow past sphere at low Reynolds number (Re=0.01)

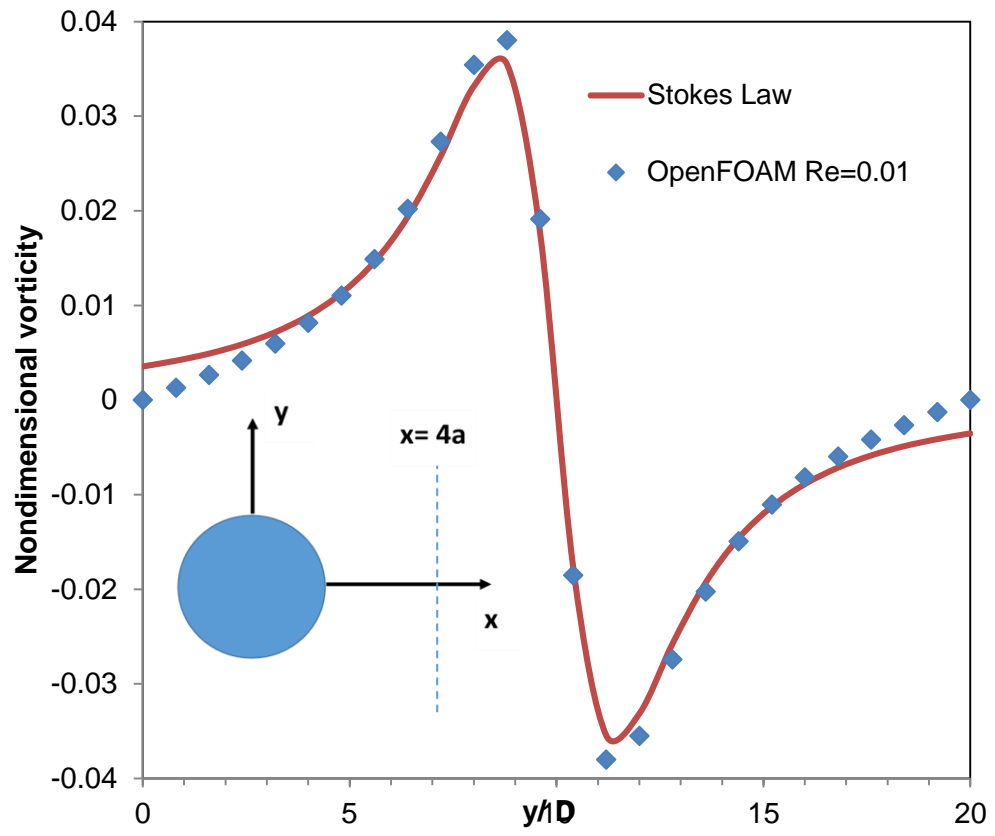Figure 9 Vorticity magnitude along y=4a for *H*=15D (Re=0.01)

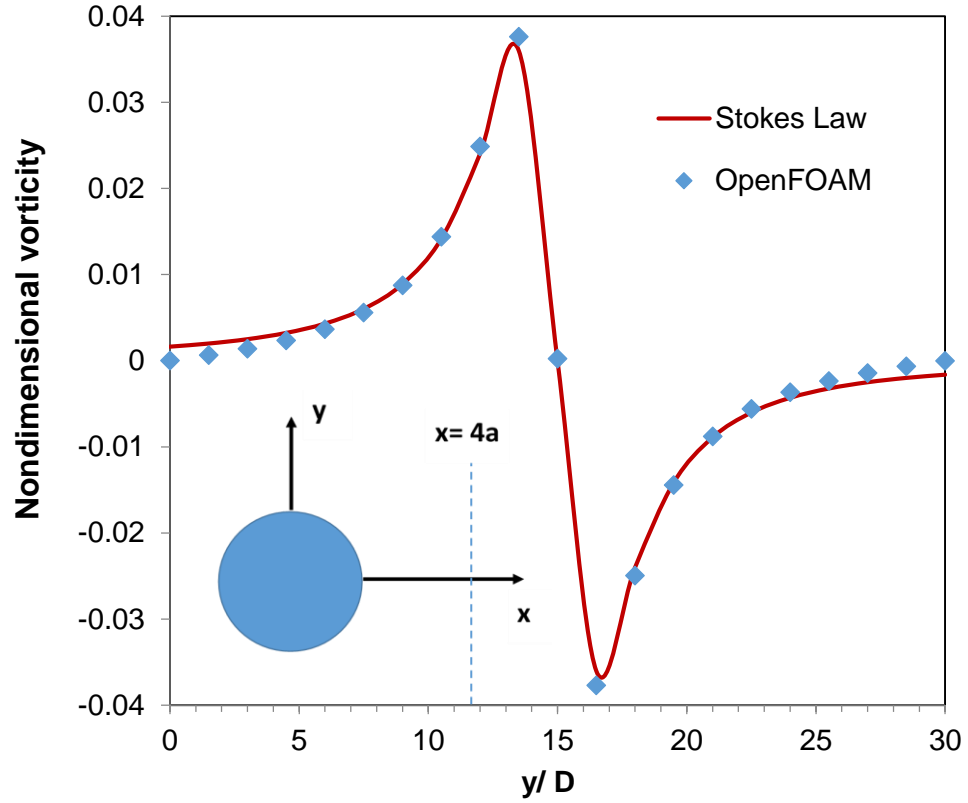Figure 10 Vorticity magnitude along y=4a for H=20D (Re=0.01)

Figure 11 Vorticity magnitude along y=4a for *H*=30D (Re=0.01)

2.2.3 Pressure

From the stokes law, the pressure for stokes flow past a sphere is

$$p = p_\infty - \frac{3}{2}\frac{\mu U a}{r^2}\cos\theta .$$ (2.23)

Here a normalized pressure is defined as pressure coefficient,

$$C_p = \frac{p - p_\infty}{\rho U^2 / 2} .$$ (2.24)

Therefore, the Stokes Law actually predicts the pressure coefficient as following,

$$C_p = \frac{-3\mu a cos\theta}{\rho U r^2} .$$ (2.25)

17

From the equation for pressure coefficient above, we can see that C_p is zero if $\theta=\pi/2$, which means the pressure coefficient is zero along the vertical axis across the sphere center. Figure 12 shows that the pressure coefficient along the y axis predicted by the simulation is nearly zero, which correspond to previous prediction.
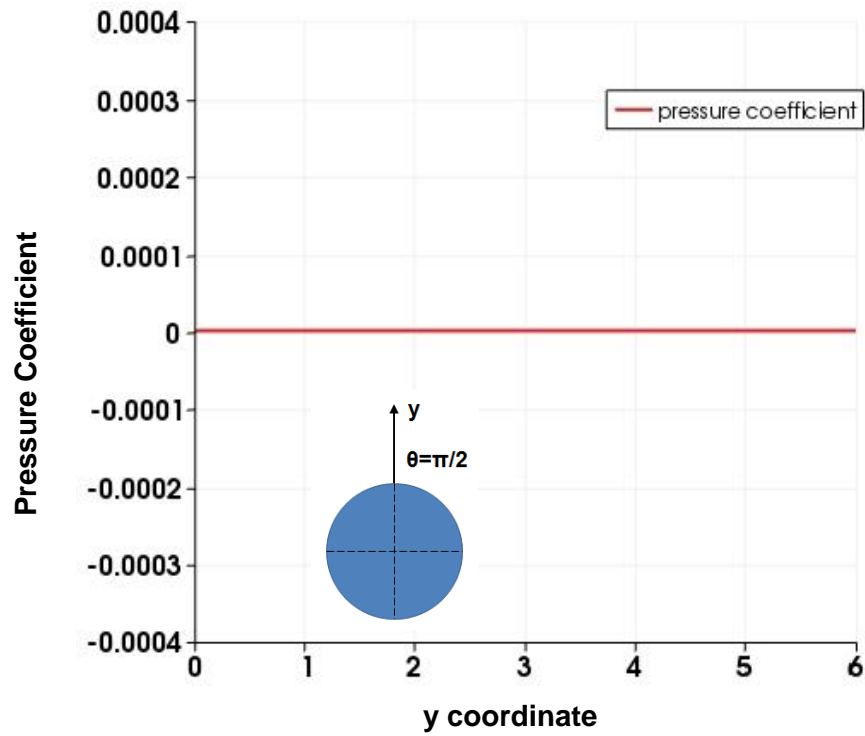

Figure 12 Pressure coefficient along the y- axis across sphere center

Figure 13 plots the pressure coefficient along the parallel line across the sphere center, where $cos\theta=-1$ when $x<0$ and $cos\theta=1$ when $x>0$. The pressure coefficient becomes,

$$C_p = \frac{-3\mu a}{\rho U x^2} = -sign(x)\frac{6a^2}{x^2 Re}.$$ (2.26)

18
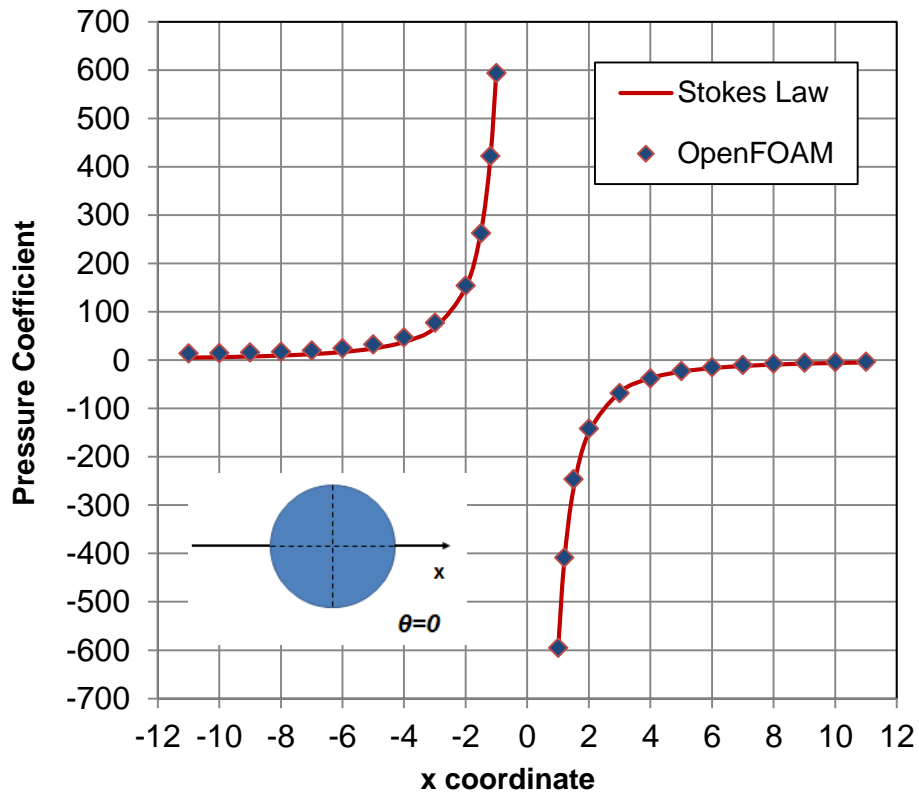
Figure 13 Pressure coefficient along the x-axis across sphere center

In summary of this chapter, by comparing with exact solutions for velocity, vorticiy and drag coefficient, OpenFOAM predict reliable situational results for a uniform flow past s sphere. As the channel goes bigger, the numerical results become more exact. After benchmark work of the code, simulations at higher Reynolds number and for flow past a spheroid will be discussed in next chapters.

3. FLOW PAST A SPHERE AT REYNOLDS NUMBER UP TO 500

At Reynolds number increasing up to 500, the flow after the sphere displays different patterns. Many researchers have reported such variations of the flow pattern observed from experiments and simulations. The first chapter of this thesis has done a review on these publications. Sakamoto and Haniu defined classifications or stages of flow according to the flow pattern, but they did not include stokes flow at very low Reynolds number (Re<<1) and flow at low Reynolds number before vortex rings appears [8]. This thesis sums up all the results and classifies six stages from very low Reynolds number up to 500. The six stages are shown in the Figure 14. Please note that the boundaries between two stages are approximate values. Table 1 shows corresponding flow characteristics and pattern pictures cited from previous publications.

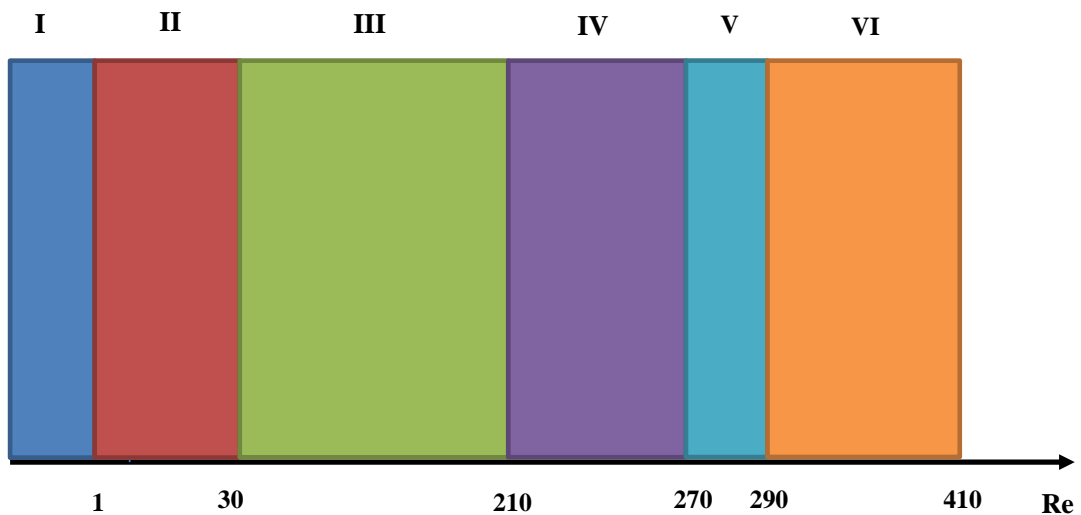Figure 14 Stages of the flow past a sphere versus Reynolds number

Table 1 Characteristics and pattern of the flow at different Reynolds numbers

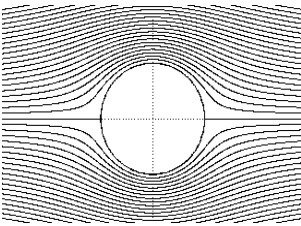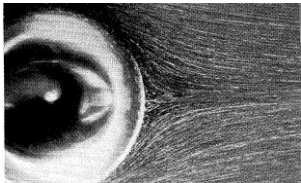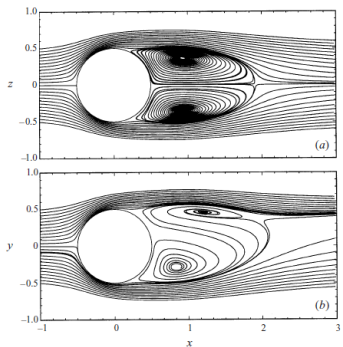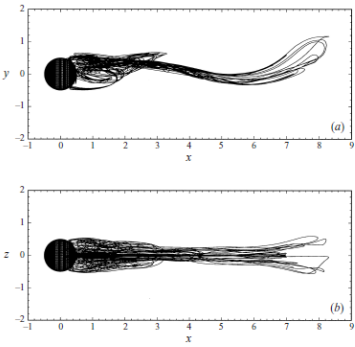| Stage	Reynolds number	Characteristics & Pattern
I	Re<< 1	**Stokes flow**
II	1<Re<30	**Single tale without rings**
III	30<Re<210	**Single thread with vortex rings**
IV	210<Re<270	**Double threads**

Table 1 Continued

Stage	Reynolds number	Characteristics & Pattern
V	$270 < Re < 290$	**Double threads with waves**
VI	$290 < Re < 410$	**Vortex loops**

From the pattern pictures in the Table 1, descriptions of the above six stages can be made as following stages.

Stage I. At very Reynolds number ($Re < 1.0$), the streamline of the flow is symmetrical both vertically and horizontally.

Stage II. A vortex sheet appears after the sphere.

Stage III. Separation begins to occur at Reynolds number around 30 and generate a wake containing two oppositely rotating rings. The wake length and separation angle should change with the Reynolds number as previous publications reported.

Stage IV. For Reynolds number from 30 up to around 210, the flow solution remains axial symmetrical. At Reynolds number 210, the flow begins to lose axial symmetry and break up into two vortex sheets while still remains planar symmetry until Reynolds number 270.

Stage V. At Reynolds number around 270 up to 290, the flow shows periodic oscillation.

Stage VI. At Reynolds number 290, the flow begins to generate vortex loops at a single frequency.

Chapter I has already discussed the Stokes flow for the stage I. The next section of this chapter continues to discuss other stages.

3.1 Wake length and wake angle versus Reynolds number

Taneda (1956) experimentally investigates the wake length and wake angle of the flow past a sphere at Reynolds number up to about 200 [2]. He found that the wake length and wake angle shows a linear relation with the logarithm of the Reynolds number. The method he employed to measure the wake length is to take photographs of streak lines formed by aluminum powder. Orszag [11] and Fornberg [7] also published their situational results for wake length and claimed correlation with Taneda's.

As the Reynolds number is larger than a critical Reynolds number, the flow after the sphere will separate and form two symmetrical vortex rings rotating in reverse directions. There is a stagnation point in the rear of the two vortex rings [11]. Hereby the wake length is defined as the nominalized distance from the rear tip of the sphere to this stagnation point, as shown in Figure 15 (a- d) plot velocities along the centerline from

the surface of the sphere. It is can be seen that the velocity increase from negative to positive at some points as Reynolds numbers are larger than 30, which means the flow does not show any vortex rings until Reynolds number reaches 30. Correspondingly, Taneda observed that the critical Reynolds number at which the vortex-ring begins to form after the sphere is about 24. Therefore, situational results by OpenFOAM well coincide with test data at this critical Reynolds number. Furthermore, depicts the two results for wake length at increasing Reynolds number. The two results show very good agreement but a small difference at Reynolds number of 100.

(a)   **Stagnation point**

(b)
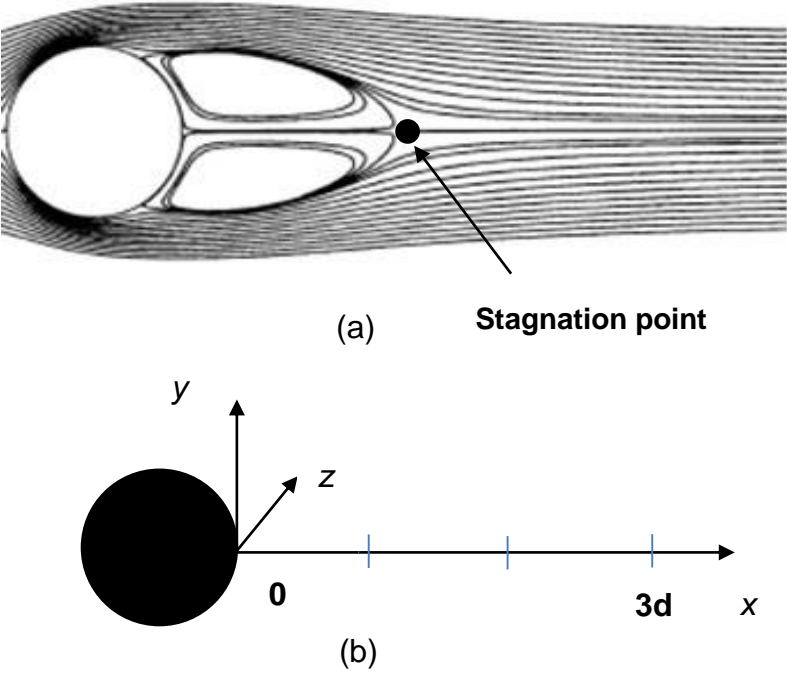
Figure 15 Nomenclature of the streamline contour and coordinate
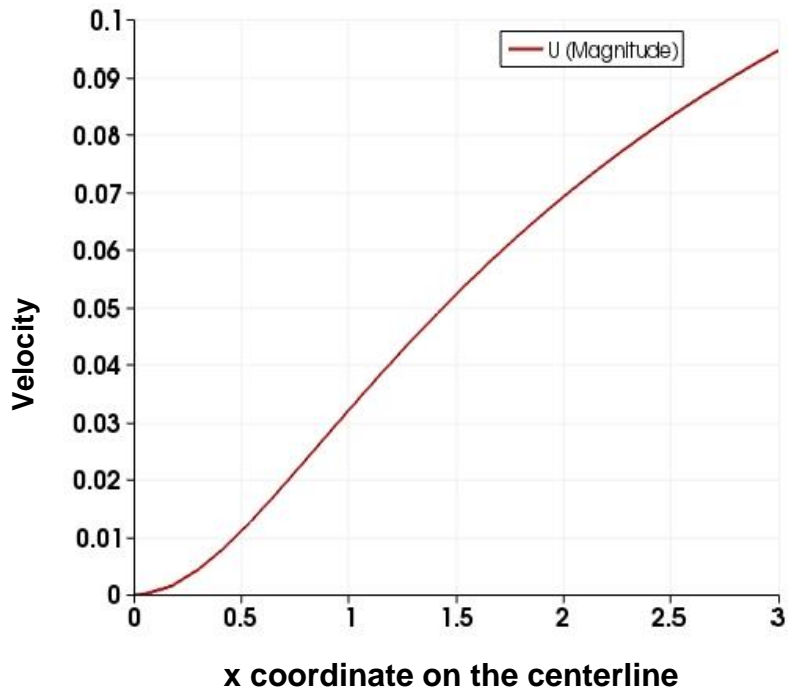
(a) Re=20
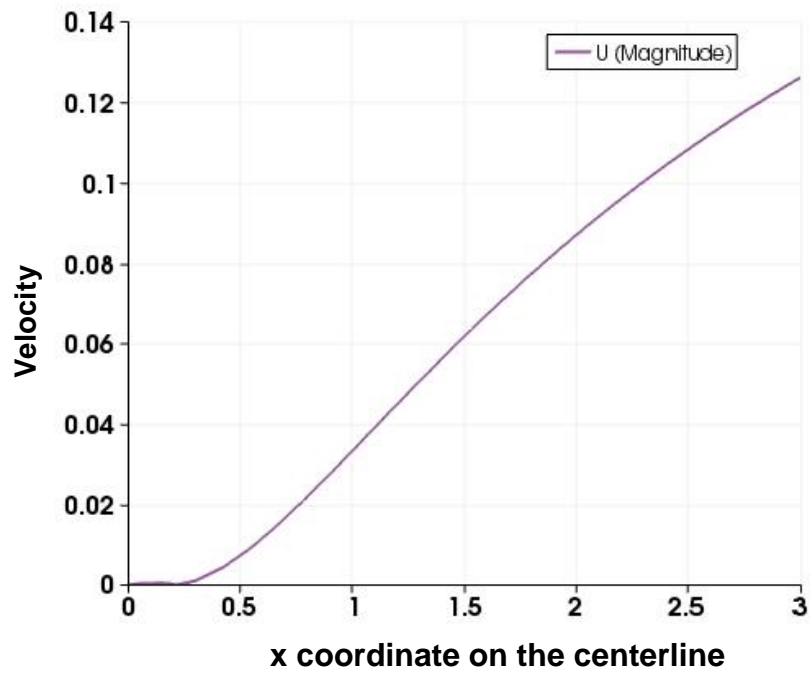
(b) Re=30

Figure 16 Velocity magnitude along the centerline after the sphere
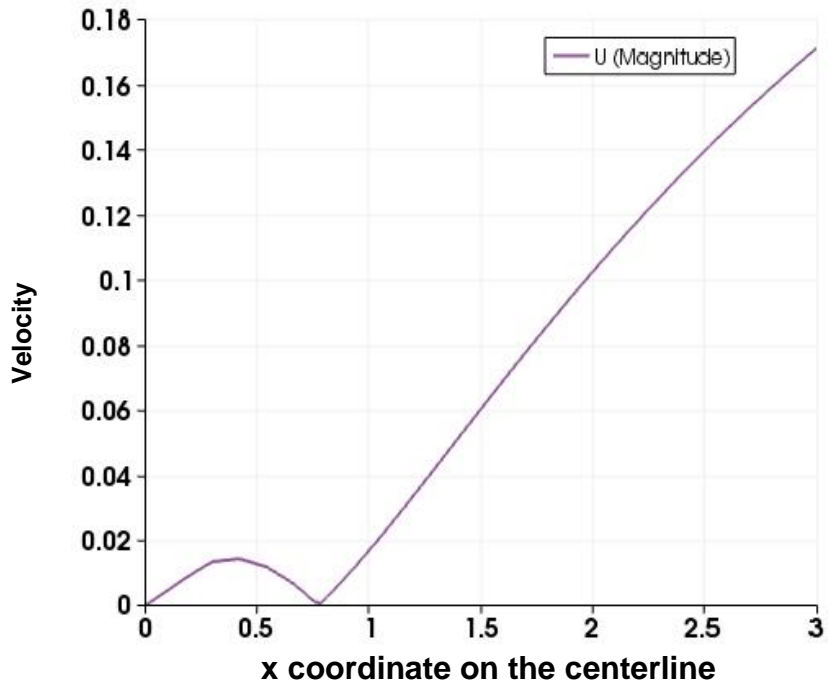
(c) Re=50
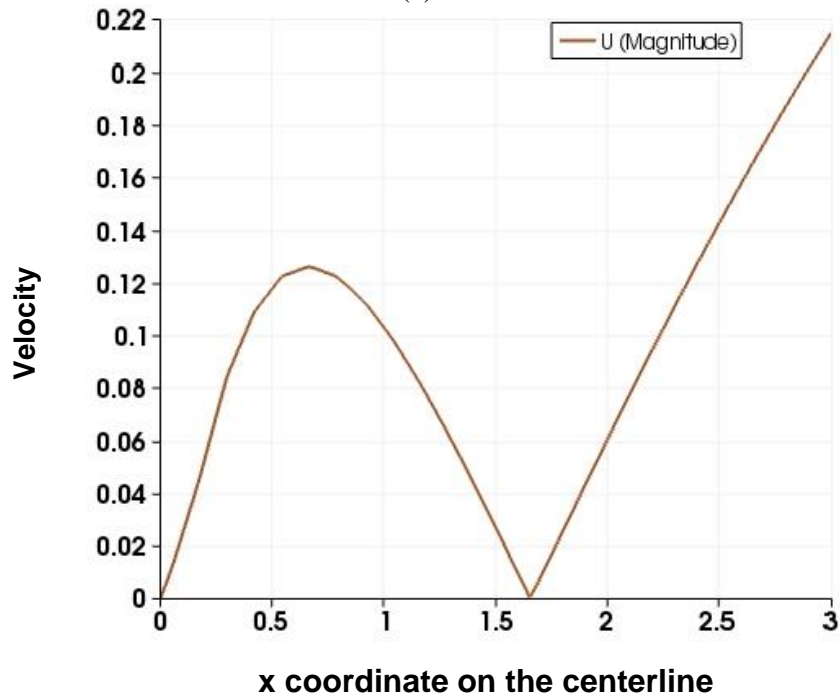
(d) Re=100

Figure 16 Continued

To investigate discrepancies of the two results at Re=100, many uncontrollable factors have to be considered. In the experiment, the flow is confronted with disturbances from its surrounding and other unavoidable error cause by test rigs or testers, while in simulations the flow is not. Similarly, the difference of wake lengths may also come from measurement since the results from Taneda are measured from photographs.
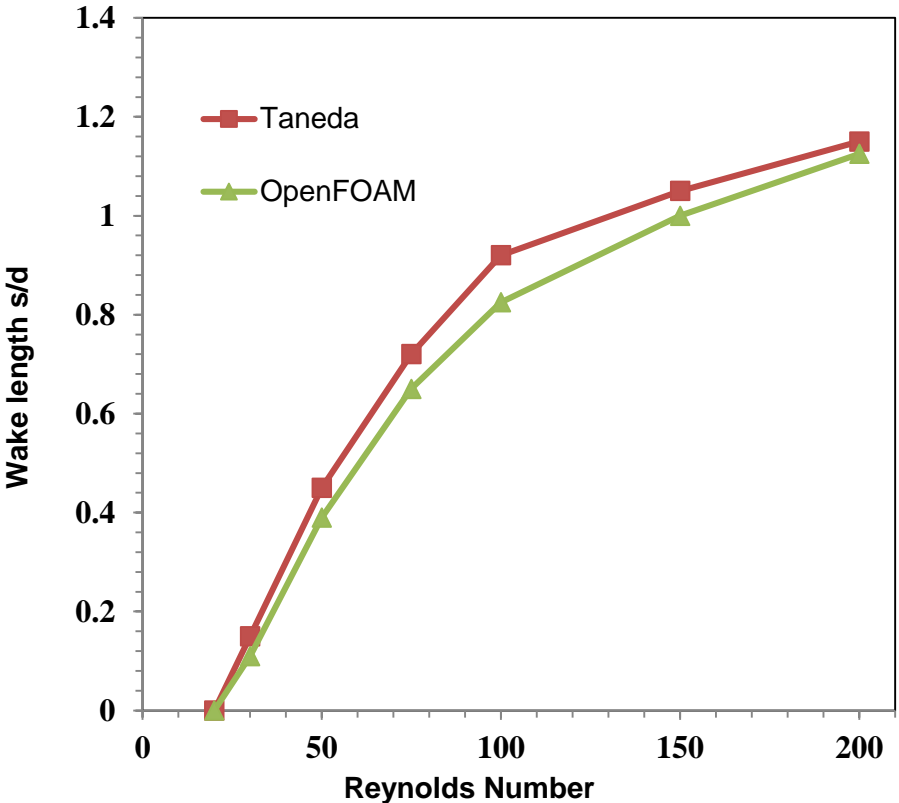
Figure 17 Wake lengths versus Reynolds number by OpenFOAM and Taneda

Figure 18 shows the streamlines plotted by OpenFOAM at four Reynolds numbers. It can be seen that the separations after the sphere expand as the Reynolds

number becomes larger and produce more pressure drag. Streamline patterns for higher

Reynolds numbers are not shown here because of instability of the flow.

Re=20   (b) Re=30

(c) Re=50   (d) Re=100
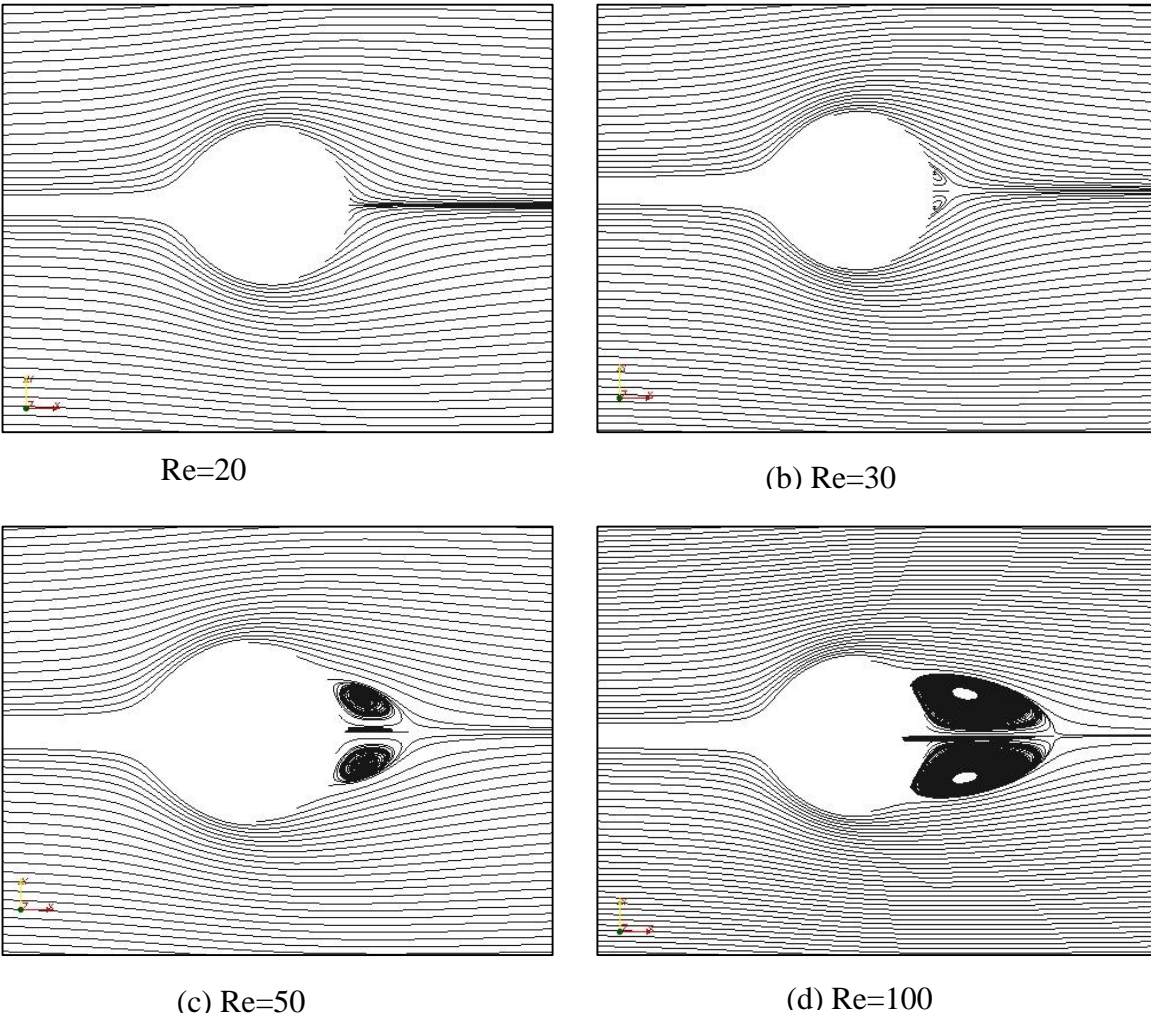
Figure 18 Flow patterns after the sphere at different Reynolds numbers

Figure 19 also shows the flow patterns for Reynolds number of 280 including

velocity magnitude and vortex contours. As Table 1 shows, at Reynolds number of 280,

the flow begin to have a wave after the sphere and the flow is symmetrical on one plane but asymmetrical on another, which is also demonstrated by Figure 19 (b) and (c).
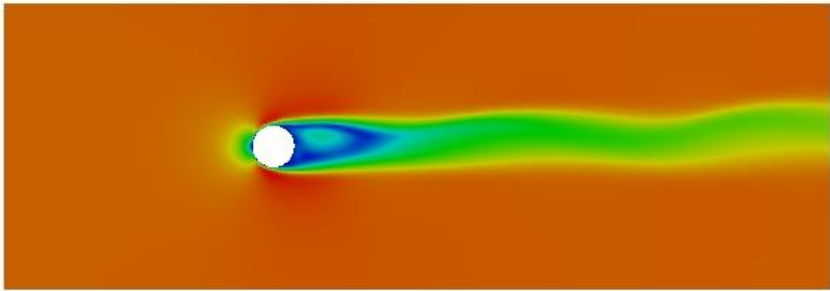
(a) Velocity magnitude
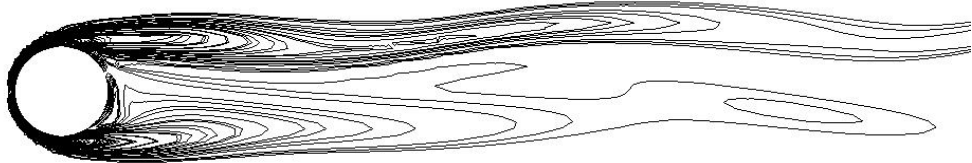
(b) Vorticity contour about z-axis
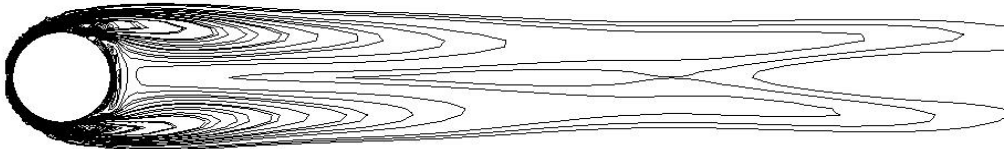
(c) Vorticity contour about y-axis

Figure 19 Velocity and vorticity fields for flow past a sphere at Re=280

3.2 Drag coefficient for flow past a sphere

Figure 20 shows the drag coefficients versus Reynolds number up to 10000 predicted by various models for flow past a sphere. It can be seen from the figure that the drag coefficient decrease rapidly at lower Reynolds number and tend to be constant at Reynolds number around 1000.
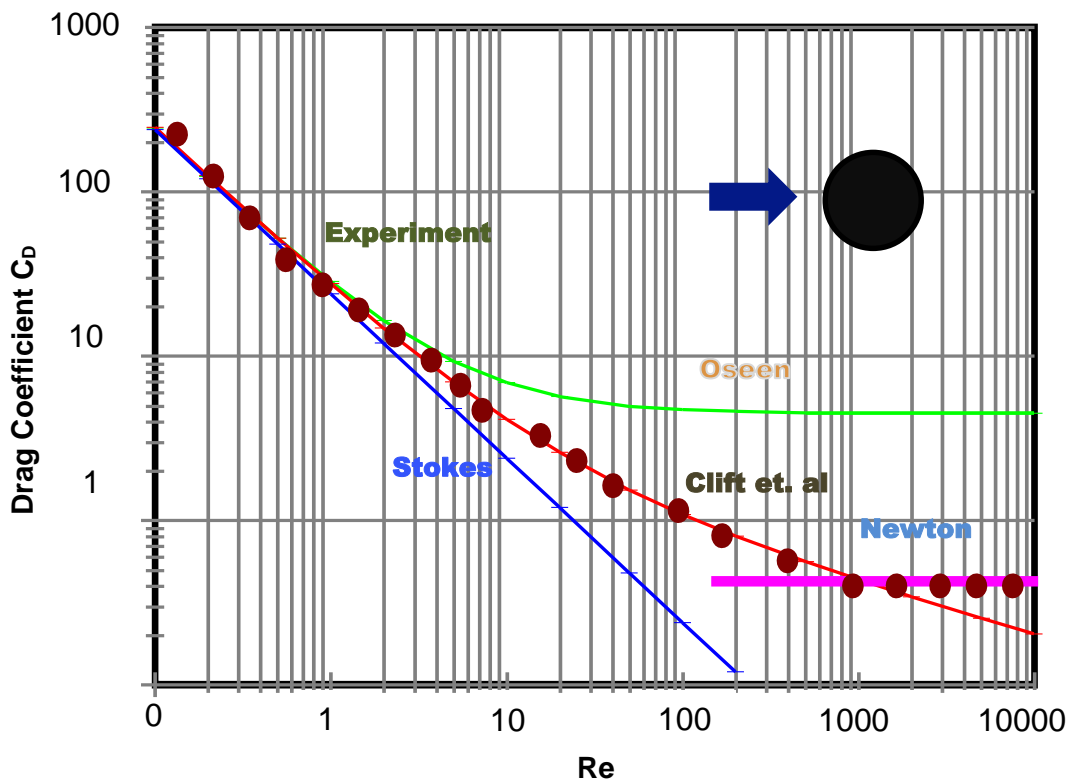
Figure 20 Predictions of various models for drag coefficient past a sphere

To find out the reason for this phenomenon, discussion would be put on sources of the drag force. The drag force on an immersed body could be composed of two parts, frictional drag (viscous drag) and pressure drag (form drag or profile drag). The

frictional drag comes from the shear stress between the fluid and the body surface. This friction force is associated with the development of the boundary layer and caused by the velocity gradient in the vertical direction, i.e., $\tau_w = -\mu \, du/dy$ in a Newtonian fluid. The pressure drag comes pressure difference between the front and rear parts of the obstacle passed by a flow at relatively higher Reynolds number (Re>20 for flow past a sphere). This drag is associated with the formation of a wake due to boundary layer separations. Both types of drags are because of viscosity since there would be no drag if the fluid is inviscid. But please also note that the two types of drags are induced by different flow phenomena. Generally speaking, frictional drag is important for attached flows and pressure drag is important for separated flows.

At very low Reynolds number, when the inertia effect is very small and hence the drag is dominated by frictional component, the body is called as streamlined body and the flow is called Stokes Flow or Creeping Flow.

In the previous chapter, flow at very low Reynolds numbers was discussed and the drag coefficient was also compared with the theoretical results from the Stokes law which predicts the drag coefficient for creeping flows:

$$C_D = \frac{24}{\text{Re}} . \tag{3.1}$$

But the Stokes law is only applicable at Reynolds number smaller than 0.5. Many researchers have been working on figuring out an approximate expression for predicting the drag coefficient on a sphere. Oseen [13] considered the inertia effects and developed a correction to the Stokes drag coefficient,

$$C_D = \frac{24(1+3\,\text{Re}/16)}{\text{Re}}. \qquad (3.2)$$

Clift et al. [14] presented an equation proven to have very good correlation with experimental data by Roos and Willmarth [5] as:

$$C_D = \frac{24}{\text{Re}}(1+0.15\,\text{Re}^{0.687}) + \frac{0.42}{1+42500\,\text{Re}^{-1.16}}. \qquad (3.3)$$

Drag coefficient. Many researchers have published the correlation for drag coefficient versus the Reynolds number in uniform flow past a sphere [20, 21, 22, 23, 24]. These correlations they claimed may differ, but as the Reynolds number goes very small all correlations lead to the same conclusion:

$$\lim_{\text{Re}_d \to 0} C_D = \frac{24}{\text{Re}_d}. \qquad (3.4)$$

Figure 21 displays the curve for drag coefficient plotted from Eqn. (3.4) and corresponding with simulation results given by OpenFOAM. OpenFOAM generally reports slight larger results. The largest difference is a little less than 2.8%. Again, this comparison proves that OpenFOAM is quite reliable,

$$C_D = \frac{D}{\rho W^2 \pi a^2} = \frac{24}{\text{Re}_d}. \qquad (3.5)$$
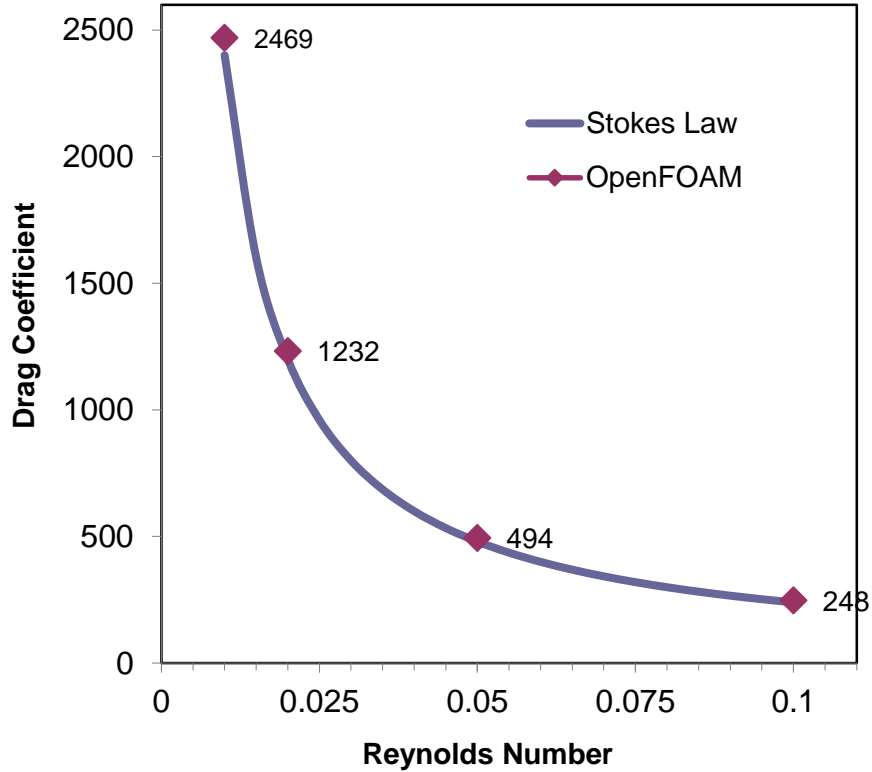
Figure 21 Drag coefficient versus Re by Stokes Law and OpenFOAM

As the angle of attack increases, boundary layer separation occurs due to high pressure gradient at top and rear parts of the body. This separation finally cause wake formation and makes pressure after the sphere drop. As a result, the pressure difference between the front and rear regions consequently increases. This is also the reason why the drag coefficient is higher for flow past a disk than a sphere, as reported in experiments by Roos and Willmarth [5]. A body is called bluff body when the drag is dominated by pressure drag.
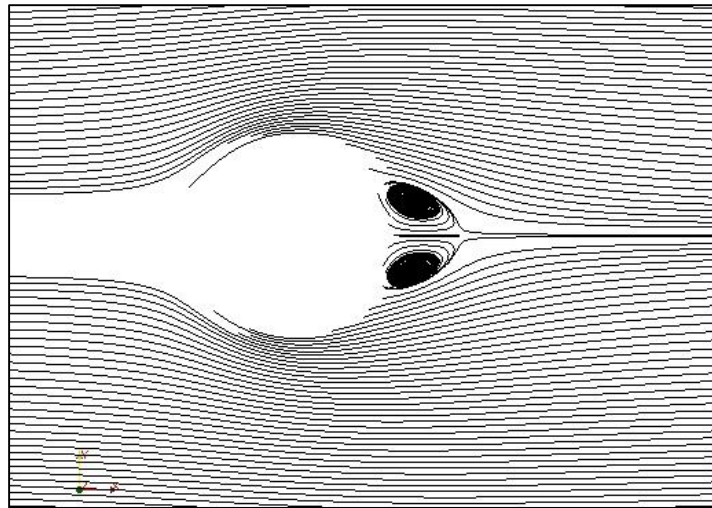
Figure 22 Streamlines of the flow past a sphere at Re=50

Figure 23 Pressure distribution of the flow past a sphere at Re=50

Chapter 2 shows the wake size increases with the Reynolds number for steady

flows past a sphere, indicating the separation zone grows larger and hence produces

more pressure drag. The pressure drag becomes more and more dominant and finally the

friction drag can be neglected at Reynolds numbers higher than 1000, and the drag

coefficient keep constant in the Newton regime, implying all the pressure is turned into eddy motion.

The following section presents drag coefficients by the CFD simulation for Reynolds number ranging from 1 to around 300, as shown in Figure 24. The situational results agrees closely with experimental data by Roos and Willmarth [5]. Both of the two drag coefficients falls rapidly before Reynolds number of 50 and then slows down decreasing afterwards.
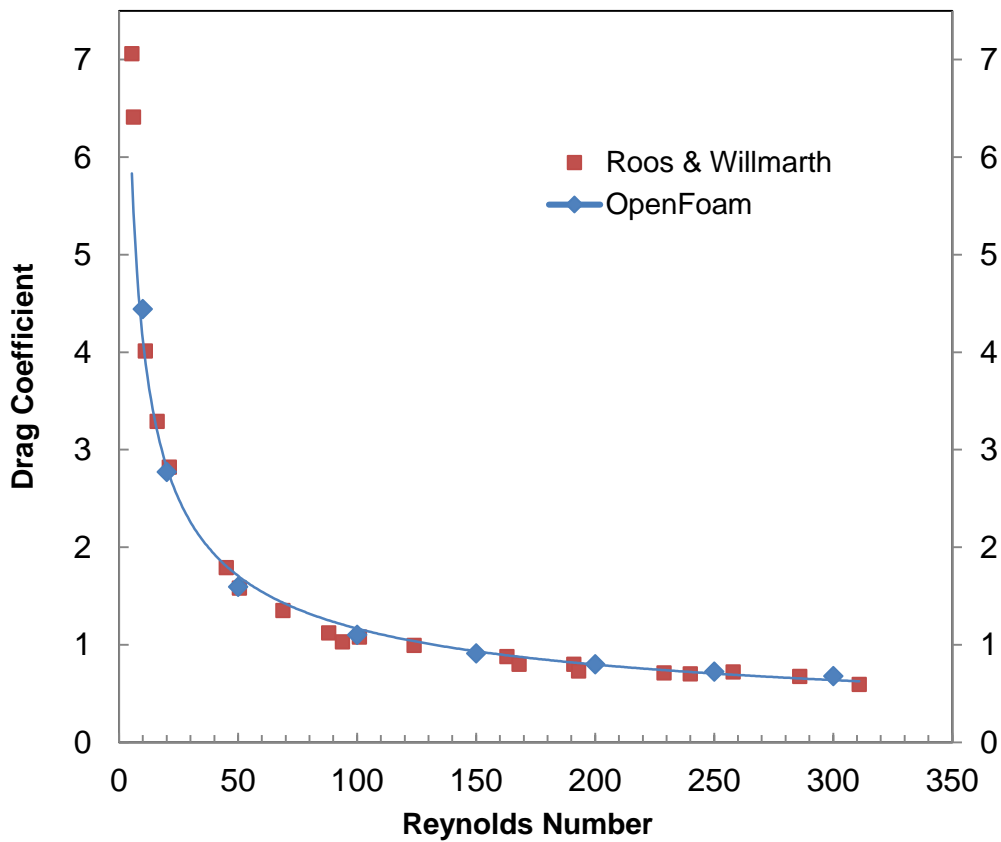
Figure 24 Drag coefficient versus Reynolds number for flow past a sphere

4. FLOW PAST A SPHEROID UP TO REYNOLDS NUMBER 400

Compared to flow past a sphere, flow past a spheroid has been more and more studied by researchers in the field of biomedical technology and navy fluid mechanics. Figure 25 shows how a typical bacterium cell looks like. Then the motion of such a bacteria in body can be modeled as flow past a spheroid. Because the cells are tiny and body blood is very viscous, the Reynolds number is very small. Biomedical researchers can also apply this fluid mechanics model in motion of a capsule since a capsule is in a similar shape of a spheroid [25].
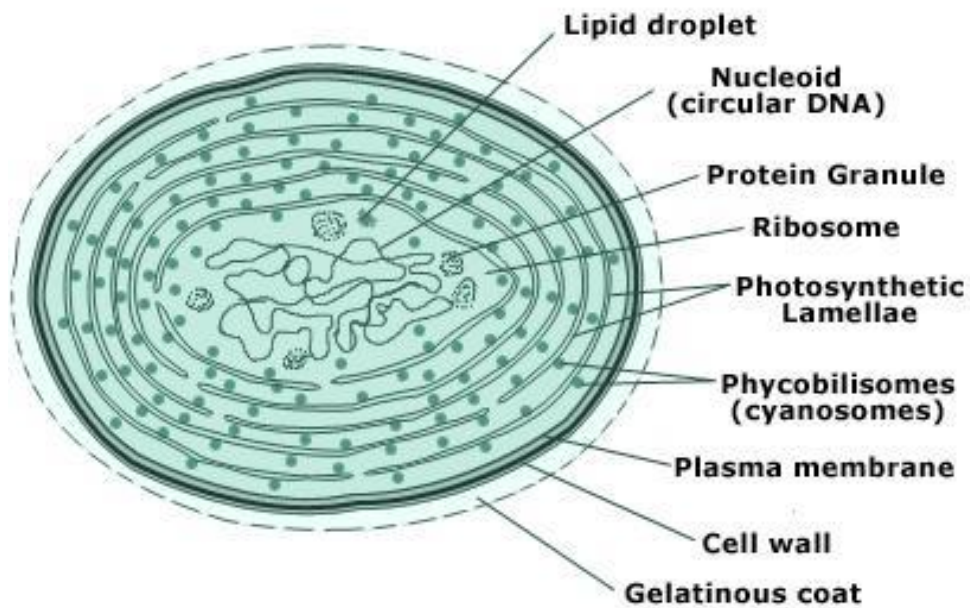
Figure 25 Structure of a bacterium cell

For naval researchers, study of this subject is important because the submarine can also be taken as a spheroid in shape. In such cases, the Reynolds number is very high since the size of a submarine is very large.
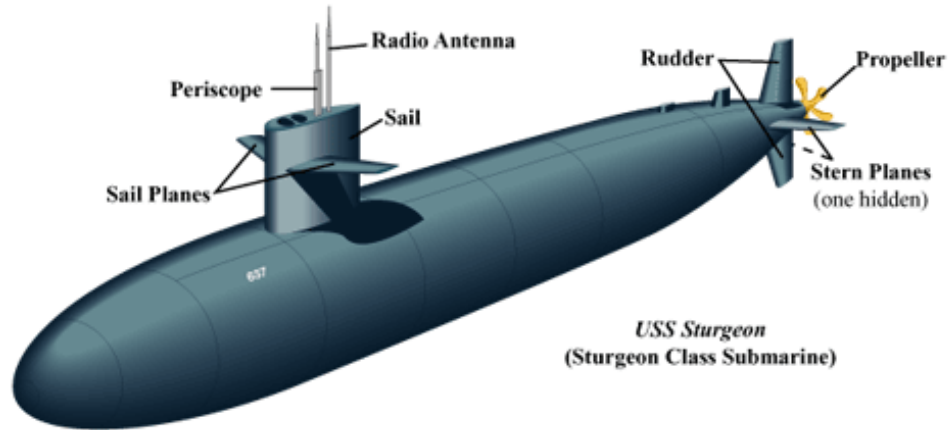
Figure 26 Exterior of a submarine

This work focuses on study of viscous flow past a spheroid at low Reynolds number.

4.1 Viscous flow past a spheroid at very low Reynolds number (Re<1)

Oseen, Aoi, and Breach [14, 15, 16] provide exact solutions for drag coefficient on a spheroid in a uniformly passing flow.

The Stokes and Oseen expansions consider the problem of viscous flow with uniform free-stream velocity U in the x direction past an ellipsoid of revolution as

$$\frac{x^2}{a^2} + \frac{r^2}{b^2} = 1 \quad (r^2 = y^2 + z^2, a \geq b).$$
(4.1)

Here the focal length 2c and eccentricity e are defined by

$$c = \sqrt{a^2 - b^2} = ea \ (0 \le e < 1).$$ (4.2)
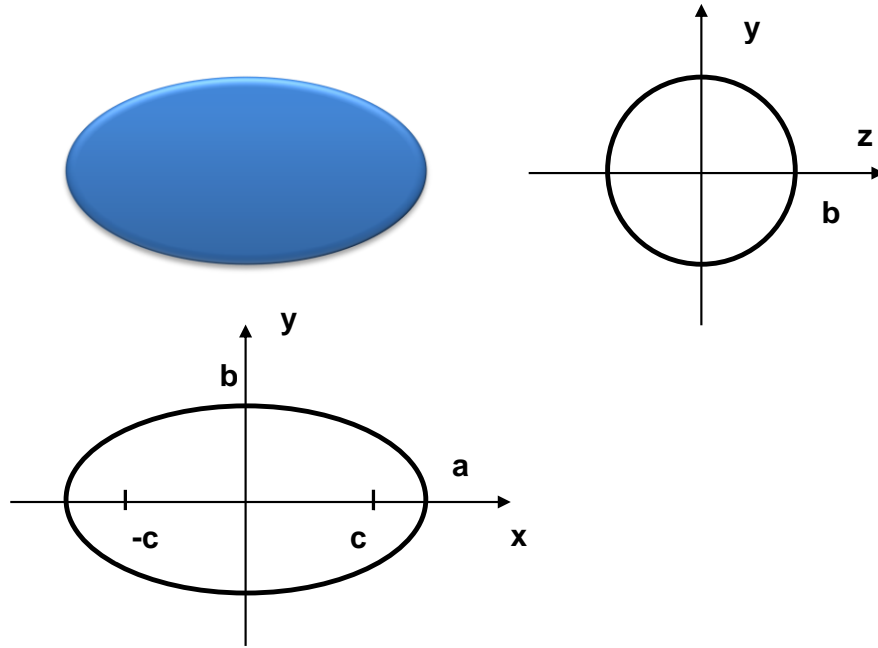
Figure 27 Nomenclature of a spheroid with top and side views

$$\mathbf{D} = \frac{32\pi\mu U a e^3}{2e + (3e^2 - 1)\log\frac{1+e}{1-e}}[1 + \frac{2e^3 R_a}{2e + (3e^2 - 1)\log\frac{1+e}{1-e}} + O(R_a{}^2)]$$ (4.3)

If $e \to 0$, namely, $b/a \to 1$, the limitation of above is

$$\lim_{e \to 0} \mathbf{D} = 6\pi\mu U a[1 + \frac{3}{8}R_a + O(R_a^2)].$$ (4.4)

When e=1, the spheroid actually becomes a sphere. Please recall that the drag

coefficient for a sphere at very low Reynolds number is $C_D = 24/\mathrm{Re}_d$ and the

corresponding drag force is $\mathbf{D}_{sphere} = C_D \rho U^2 \pi d^2 / 8 = 6\pi\mu r$, where r is the radius of the

sphere. It can be seen that $\mathbf{D}_{sphere}$ coincides with the equation (25) as R_a is very small.
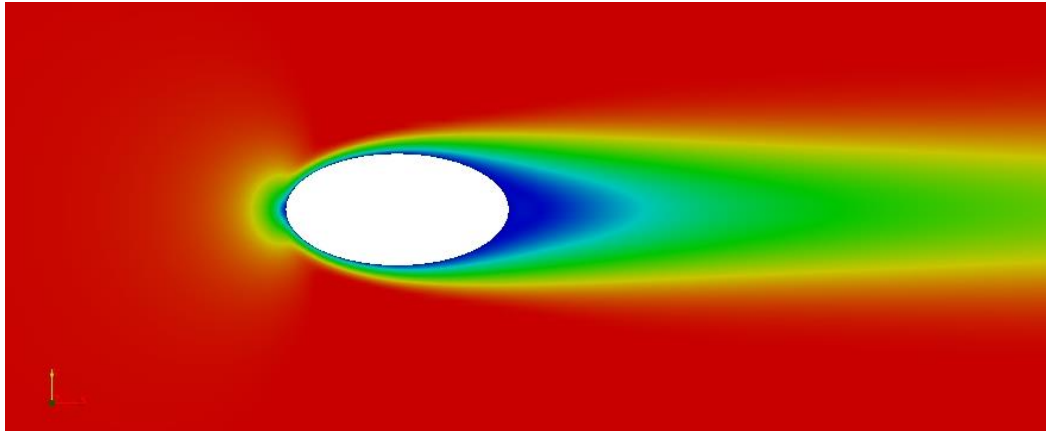
Figure 28 Velocity of flow past a spheroid with aspect ratio of 2 at Re=200
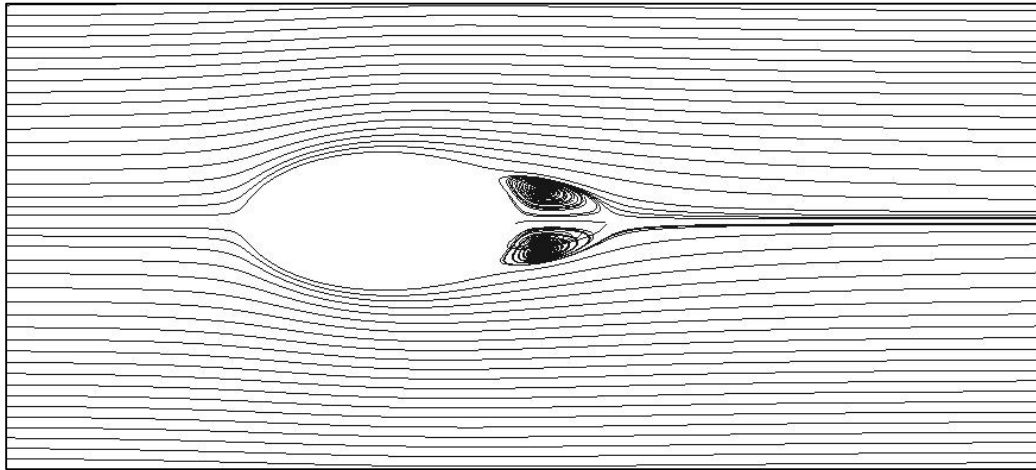
Figure 29 Streamline of flow past a spheroid with aspect ratio of 2 at Re=200

Figure 30 plots drag coefficients versus the Reynolds number based on the minor

axis length for three spheroids. The maximum Reynolds number studied here is 0.1 and

can be called the creeping flow or Stokes flow. The solid lines are calculated from the

Equation 24 and the circled dots are results by present simulation. The simulation shows

excellent agreement at aspect ratio of 2. For larger aspect ratios, there are small

discrepancies.
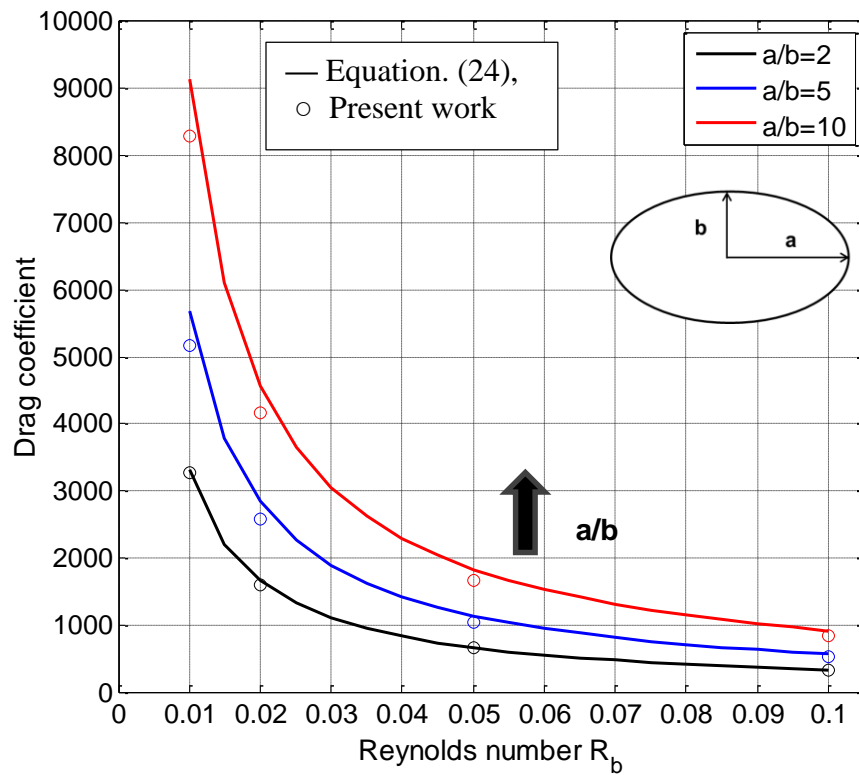
Figure 30 Drag coefficients at very low Reynolds numbers on spheroids

4.2 Flow past a spheroid at higher Reynolds number (1<Rb<500)

Masliyah and Epstein [18] presented numerical study of steady flow past oblate

and prolate spheroids for Reynolds number up to 100. They found that the drag

coefficient for oblate spheroids does not necessarily increases with the aspect ratio. In

another word, a more disk-like shape does not always mean higher drag coefficient. Actually their results reveal that at lower Reynolds numbers the drag coefficient is lower for spheroids with smaller aspect ratio. Then the drag coefficient begins to increase with the aspect ratio when the Reynolds number is larger than a certain value (e.g., around 30 for aspect ratio of 0.2) [18]. However, the publication did not find such kind of transmission for spheroids for Reynolds number up to 100. To investigate the case of the flow past a spheroid, this thesis has simulated a viscous incompressible flow past a spheroid for Reynolds number up to 1000 based on the minor axis.

Figure 31 demonstrate a uniform flow past spheroids of four aspect ratios at Reynolds number up to 500 where aspect ratio of 1 refer to a sphere. In the region studied here, the drag coefficient decreases with the Reynolds number as the boundary layer gets thinner. The decreasing speed slows down when the Reynolds number grows. For a sphere, the drag coefficient keeps almost constant ($C_D \approx 0.4$) between $10^3 < Re <$ 2.5×10^5 which is referred to as the Newton regime [26].

As can be seen from the figure, flows past spheroids of aspect ratio 1, 2, 5 and 10 also show such a decreasing tendency. However, the present simulation shows an intersection of the curves at the Reynolds number of about 400 for the sphere and the spheroid with an aspect ratio of 2. Before the crossing, the drag coefficient increases with the aspect ratio. The more slender the spheroid is the higher drag coefficient it produces, so the sphere has the lowest drag coefficient. While after the crossing, the sphere reports a higher drag coefficient than the spheroid with aspect ratio of 2.
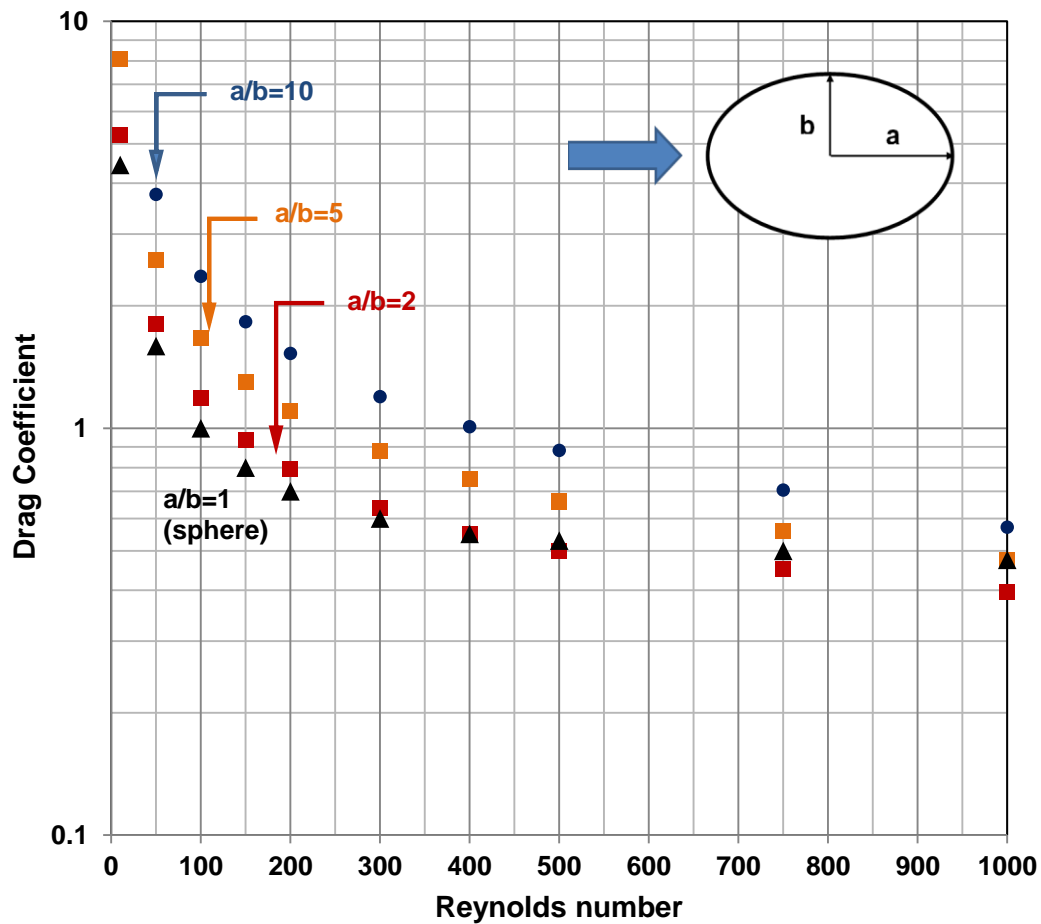
Figure 31 Drag coefficient for flow past a spheroid up to Reynolds number of 500

The curve of sphere decreases very slowly at Reynolds number of 400 where the curves for prolate spheroids (a/b>1) are still dropping significantly. Therefore, the present study predict that the spheroids have a lower constant drag coefficient than the sphere ($C_D<0.4$) at higher Reynolds number.

The crossing of the curves in Figure 32 can be explained from constitution of the total drag. The total drag experienced by the object includes frictional drag and form drag (or pressure drag). The frictional drag is due to the shear stress between the flow and the solid surface at the interface while pressure drag is because of pressure

difference generated by flow motion. For any arbitrary object, the frictional drag on it always decreases with Reynolds number and tend to be negligible compared to pressure drag at high Reynolds number. However, the growth of pressure drag differs for different body shapes. Some bodies, such as spheroids, on which the pressure drag is small, can be called streamlined body; while for other bodies who experience large pressure drag are called blunt body, such as plate.

As discussed in the previous chapter, the pressure drag becomes more and more dominant as the Reynolds number grows, finally making the drag coefficient curve reach a constant region where all the pressure loss after the body is due to the eddy motion. The larger the wake region is, the more pressure drag the sphere will experience. However, at same Reynolds numbers, the size of the wake region for a spheroid is smaller than a sphere [18].

To sum up the discussion, the spheroid has larger frictional drag and hence lower drag coefficients at lower Reynolds numbers where the frictional drag is dominant and spheroid has larger surface area for friction. To the contrary, at the higher Reynolds number the pressure drag becomes dominant and the spheroid has smaller drag coefficients because of smaller separation areas.
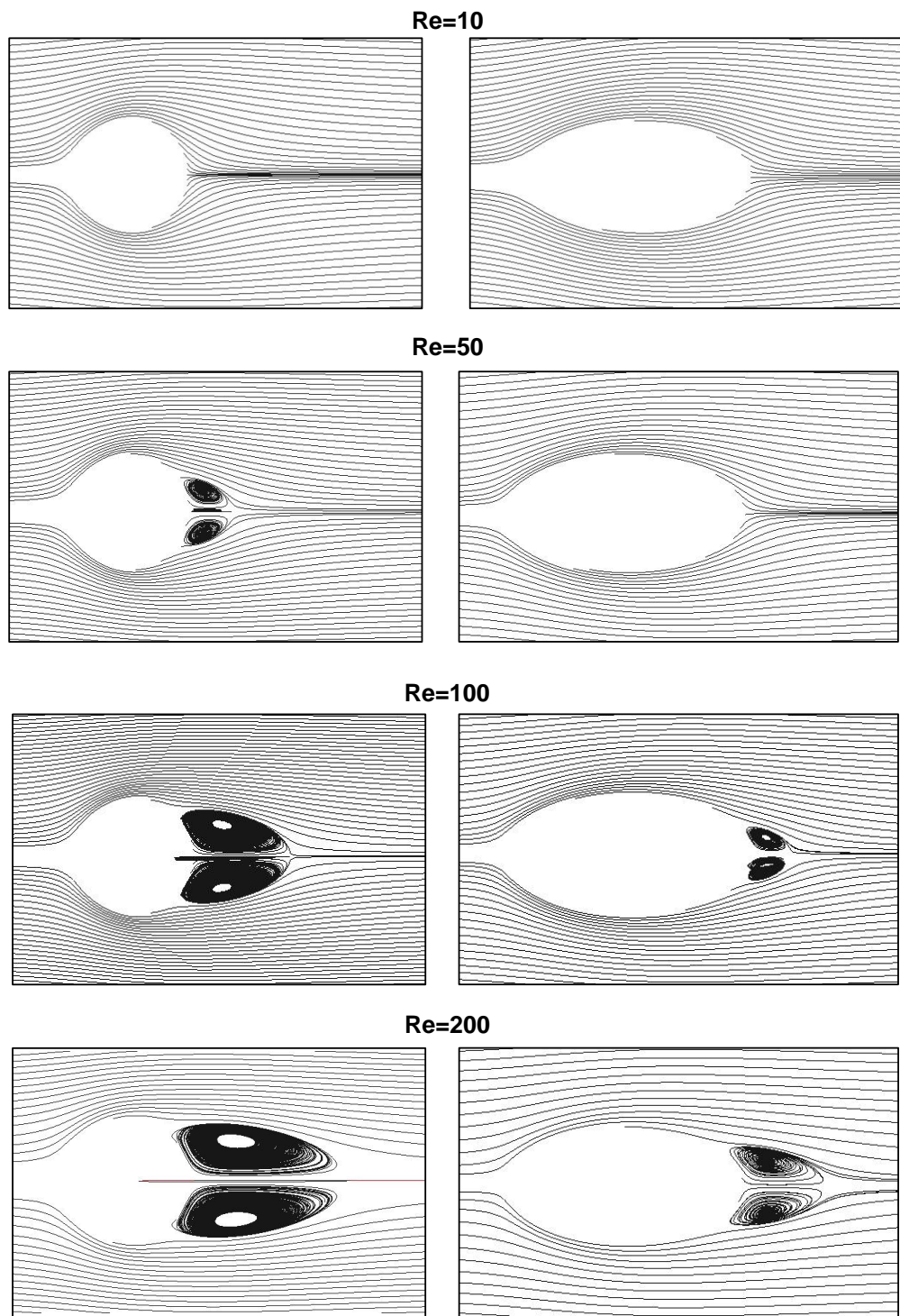
Re=10

Re=50

Re=100

Re=200

Figure 32 Streamlines on a sphere and a spheroid at four different Reynolds numbers

44

4.3 Convergence study and mesh dependence of the simulation

Convergence is critically important for a CFD simulation. It is important to remember that a numerical simulation can only obtain approximations but never the exact solutions forever. The objective of a simulation is to yield reliable results for people. The word "reliable" here depends on how much accuracy does the CFD user need. The more accurate a solution is demanded, the longer time or stronger hardware the computation cost. Sometimes it is not necessary to seek for highly accurate results in case that "reliable" means fairly accurate.

Mesh density plays an important role in CFD simulations. An ideal meshed model should have independence of mesh sizing, i.e., the results does not change no matter how denser the mesh is changed. In reality, it is difficult to achieve a mesh independent solution even the smallest mesh available is applied. An economy way to do a simulation is to consider both mesh independence and computation efficiency. The CFD user should try to reduce the cost of a computation as far as the results controlled in the range satisfying the requirement of accuracy. Figure 34 shows the drag coefficient for flow past a sphere at Reynolds number of 50 computed by four simulations with increasing mesh density. By increasing the number of the mesh cells, it can be seen that the simulation with over 1 million cells results in a value showing good consistency with the previous case. This indicates that the simulation with over 1 million cells has reached a solution that is independent of the mesh resolution, and we can use the 0.9 million case for further analysis, since it provides a result within an acceptable difference.
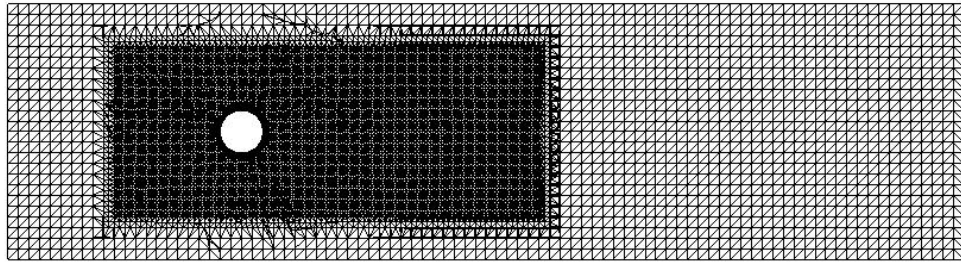
Figure 33 Meshed model for a channel with a sphere
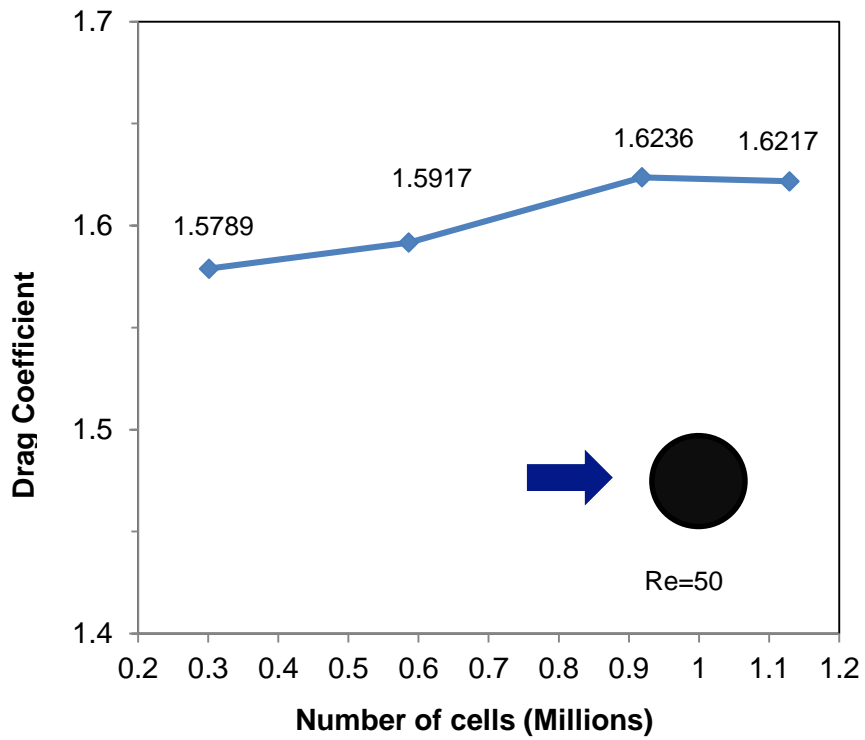
Figure 34 Drag coefficients versus number of cells for flow past a sphere at Re=50

Figure 35 records variations of calculated drag coefficients with the time step for the four cases. With time step increases, all of the four results tend to converge and become constant at time step of around 50. It is also interesting to see that the speed of convergence is not relative to the mesh density. A finer meshed model means more computation, while coarser meshes take longer time to converge.
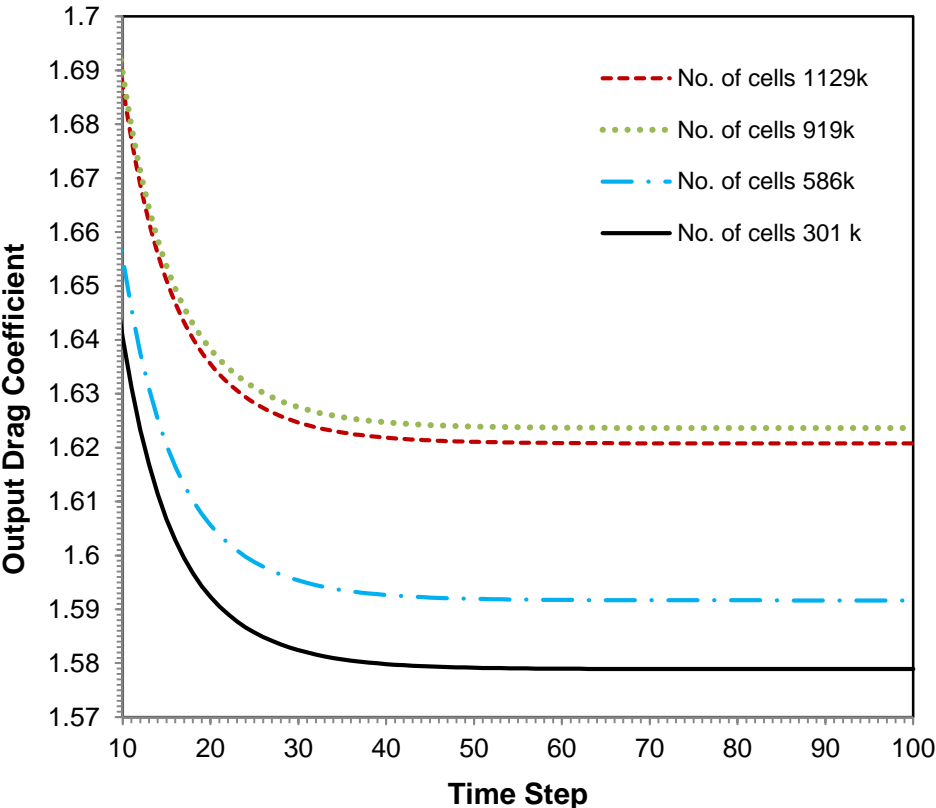
Figure 35 Drag coefficients by four simulations versus time step

REFERENCES

[1] H. Lamb, 1945, *Hyrodynamics*, University Press, Cambridge, England.

[2] S. Taneda, 1956, "Experimental Investigation of the Wake behind a Sphere at Low Reynolds Numbers,"J. Phys. Soc. Japan, **11**, 1104-1108.

[3] R.H. Magarvey & R.L. Bishop, 1961, "Wakes in Liquid-liquid Systems," Phys. Fluids **4**, 1418-1422.

[4] Y. Rimon & S.I. Cheng, 1969, "Numerical Solution of a Uniform Flow over a Sphere at Intermediate Reynolds Numbers," Phys. Fluids, **12**, 949- 959**.**

[5] F.W. Roos, & W. W. Willmarth, 1971, "Some Experimental Results on Sphere and Disk Drag," AIAA J., **9**, 285-291.

[6] I. Nakamura, 1976, "Steady Wake Behind a Sphere," Phys. Fluids **19**, 5-8.

[7] B. Fornberg, 1988, "Steady Viscous Flow Past a Sphere at High Reynolds Numbers," J. Fluid Mech. **190**, 471-489.

[8] H. Sakamoto & H. Haniu, 1995, "A Study on Vortex Shedding from Spheres in a Uniform Flow," J. Fluid Eng. **112**, 386-392.

[9] H. Sakamoto & H. Haniu, 1995, "The Formation Mechanism and Shedding Frequency of Vortices from a Sphere in Uniform Shear Flow," J. Fluid Mech. **287**, 151- 171.

[10]   T. A. Johnson & V.C. Patel, 1999, "Flow Past a Sphere up to a Reynolds Number of 300," J. Fluid Mech., **378**, 19-70.

[11]   A.G. Tomboulides & S.A. Orszag, 2000, "Numerical Investigation of Transitional and Weak Turbulent Flow Past a Sphere," J. Fluid Mech., **416**, 45-73.

[12]   A. Oberbeck, 1910, "Über Die Stokessche Formel Und Über Die Verwandte Aufgabe in Der, Hydrodynamik," Arkiv Math. Astron. Fys., **6**, No. 29.

[13]   C. W. Oseen, 1927, *Neuere Methoden und Ergebnisse in der Hydrodynamik*, Leipzig, Germany.

[14]   Clift R, Grace JR & Weber ME. , 1978, *Bubbles, drops, and particles*. Academic Press, New York.

[15]   T. Aoi, 1955, "The Steady Flow of Viscous Fluid past a Fixed Spheroidal Obstacle at Small Reynolds Numbers," J. Phys. Soc. Japan, **10 (2)**, 121- 129.

[16]   D. R. Breach, 1961, "Slow Flow Past Ellipsoids of Revolution," J. Pluid Mech., **10**, 306-314.

[17]   Y. Rimon & H.J. Lugt, 1969, "Laminar Flows Past Oblate Spheroids of Various Thicknesses," Phys. Fluids, **12**, 2465- 2472.

[18]   J. H. Masliyah & N. Epstein, 1970, "Numerical Study of Steady Flow Past Spheroids," J. Fluid Mech., **44**, 493- 512.

[19]   A.T. Chwang & T.Y. Wu, 1976, "Hydromechanics of Low-Reynolds-number Flow. Part 4. Transition of Spheroids," J. Fluid Mech., **75**, 677-689.

[20]   H. Schlichting, 1955, *Boundary Layer Theory*, McGraw-Hill, New York.

[21]   M. M. Denn, 1980, *Process Fluid Mechanics*, Prentice-Hall: Englewood Cliffs, New Jersey.

[22]   R. B. Bird, W. Stewart & E. Lightfoot, 2002, *Transport Phenomena, 2nd edition*, John Wiley & Sons, New York.

[23]   C. J. Geankoplis, 2003, *Transport Processes and Unit Operations, 4th edition*, Prentice Hall: Englewood Cliffs, New York.

[24]   F. A. Morrison, 2013, *Introduction to Fluid Mechanics*, Cambridge University Press, New York.

[25]   C.Jeananda, (1998), *Bacterium*, Retrieved September 17, 2013 from http://www.enchantedlearning.com/subjects/bacterium/

[26]   T. Benson, (2010, September 23), *The Beginner's Guide to Aeronautics*, Retrieved September 17, 2013 from http://www.grc.nasa.gov/WWW/k-12/airplane/dragsphere.html

APPENDIX A

The Naiver-Stokes equations for a viscous incompressible fluid are:

$$\nabla \bullet \mathbf{u} = 0, \tag{1}$$

$$(\mathbf{u} \bullet \nabla)\mathbf{u} = -\frac{\nabla p}{\rho} + \nu\nabla^2\mathbf{u}. \tag{2}$$

Introducing Stokes variables:

$$x^* = x/a,\; y^* = y/b,\; z^* = z/b, \tag{3}$$

and non-dimensionalizing the velocity vector and pressure

$$\mathbf{u}^* = \mathbf{u}/U,\; p^* = b(p - p_\infty)/\mu U, \tag{4}$$

where p_∞ is the pressure at the infinity.

Then the dimensionless Navier-Stokes equations become

$$\frac{b}{a}\frac{\partial u^*}{\partial x^*} + \frac{\partial v^*}{\partial y^*} + \frac{\partial w^*}{\partial z^*} = 0, \tag{5}$$

$$R_b(\frac{b}{a}u^*\frac{\partial}{\partial x^*} + v^*\frac{\partial}{\partial y^*} + w^*\frac{\partial}{\partial z^*})\mathbf{u}^* = -(\frac{b}{a}\mathbf{e}_x + \mathbf{e}_y\frac{\partial}{\partial y^*} + \mathbf{e}_z\frac{\partial}{\partial z^*})p^*$$
$$+(\frac{b^2}{a^2}\frac{\partial^2}{\partial x^{*2}} + \frac{\partial^2}{\partial y^{*2}} + \frac{\partial^2}{\partial z^{*2}})\mathbf{u}^* \tag{6}$$

where $R_b = \dfrac{Ub}{\nu}$ is the Reynolds number respect to the semi-minor axis b.

Correspondingly, another Reynolds number $R_a = \dfrac{Ua}{\nu}$ is the Reynolds number based on the semi-major axis a. Following the ideas of Kaplun and Lagerstrom [1], assume the inner expansions for velocity and pressure to have the form:

50

$$\mathbf{u}^* = \mathbf{u}_0^* + \mathbf{u}_1^* + \mathbf{u}_2^* + ..., \tag{7.1}$$

$$p^* = p_0^* + p_1^* + p_2^* + ... \tag{7.2}$$

,where $\mathbf{u}_0^*, p_0^*, \mathbf{u}_1^*, ...$ are functions of (x^*, y^*, z^*), R_a and R_b.

$$\mathbf{u}_{n+1}^* / \mathbf{u}_n^* \to 0, \ p_{n+1}^* / p_n^* \to 0 \ \text{ as } \ R_b \to 0. \tag{7.3}$$

Obviously, this inner expansion will satisfy the Naiver-Stokes Equation with the nonlinear term is zero or Stokes Equations:

$$\nabla \bullet \mathbf{u}_0^* = 0, \tag{8.1}$$

$$\nabla p_0^* = \mu \nabla^2 \mathbf{u}_0^* . \tag{8.2}$$

Now introducing the Oseen variables

$$x = Ux / \nu = R_a x^*, \ y = R_b y^*, \ \tilde{z} = R_b z^* \ \text{ and } \ p = (p - p_\infty) / \rho U^2, \tag{8.3}$$

then the Naiver- Stokes Equations in outer variables are obtained

$$\nabla \bullet \mathbf{u}^* = 0, \tag{9.1}$$

$$(\mathbf{u}^* \bullet \nabla)\mathbf{u}^* = -\nabla p + \nabla^2 \mathbf{u}^*. \tag{9.2}$$

And the surface of the prolate sphere becomes

$$\left(\frac{bx}{a}\right)^2 + \tilde{r}^2 = R_b^2 . \tag{10}$$

As the Reynolds number R_b tends to zero, the velocity vector $\mathbf{u}^*$ at any fixed point will tend to be the free-stream value $\boldsymbol{e_y}$

$$\mathbf{u}^* = e_y + q_1 + q_2 + ... \quad , \tag{11.1}$$

$$p = p_1 + p_2 + ..., \qquad , \tag{11.2}$$

where $q_{n+1}/q_n \to 0$, $p_{n+1}/p_n \to 0$ as $R_b \to 0$.

Substitute equations (11) into (9) to yield

$$\nabla \cdot q_1 = 0, \tag{12.1}$$

$$\partial q_1 / \partial y = -\nabla p_1 + \nabla^2 q_1. \tag{12.2}$$

The no-slip boundary condition on the spheroid surface gives

$$\mathbf{u}^* = 0 \text{ on } x^{*2} + r^{*2} = 1. \tag{13}$$

Chwang and Wu [19] show that the solution for the flow past a spheroid can be constructed by a line distribution of stokeslets and potential doublets between the foci $x=-c$ and $x=c$ given by

$$
\begin{aligned}
\mathbf{u} &= U_1 \mathbf{e}_x + U_2 \mathbf{e}_y - \int_{-c}^{c} [\alpha_1 U_S (\mathbf{x} - \zeta) \mathbf{e}_x + \alpha_2 U_S (\mathbf{x} - \zeta) \mathbf{e}_y] d\zeta \\
&+ \int_{-c}^{c} [(c^2 - \zeta^2)][\beta_1 U_D (\mathbf{x} - \zeta) \mathbf{e}_x + \beta_2 U_D (\mathbf{x} - \zeta) \mathbf{e}_y] d\zeta
\end{aligned}
\tag{14}
$$

$$p = -\int_{-c}^{c} \alpha P_S (\mathbf{x} - \vec{\zeta}) \mathbf{e}_x d\zeta \ , \tag{15}$$

where $\vec{\zeta} = \zeta \mathbf{e}_x$.

The verify the no-slip boundary condition on the spheroid surface, $\mathbf{u}$ is written in the integrated form of $\mathbf{u}$, which is

$$
\begin{aligned}
\mathbf{u} &= U_1 \mathbf{e}_x + U_2 \mathbf{e}_y - (2\alpha_1 \mathbf{e}_x + \alpha_2 \mathbf{e}_y) B_{1,0} - (\alpha_1 r \mathbf{e}_r + \alpha_2 y \mathbf{e}_x) \left(\frac{1}{R_2} - \frac{1}{R_1} \right) \\
&+ (\alpha_1 r \mathbf{e}_x - \alpha_2 y \mathbf{e}_y) r B_{3,0} + \nabla \left\{ -2\beta_1 B_{1,1} + \beta_2 y \left[\frac{x-c}{r^2} R_1 - \frac{x+c}{r^2} R_2 + B_{1,0} \right] \right\}
\end{aligned}
\tag{16}
$$

where $\mathbf{e}_r = (y\mathbf{e}_y + z\mathbf{e}_z)/r$ is the unit radial vector in the y, z plane, α and β represent the mangnitute and directions of the stokeslet and doublet respectively,

$$R_1 = [(x+c)^2 + r^2]^{1/2}, \ R_2 = [(x-c)^2 + r^2]^{1/2},$$

(17.1)

$$B_{1,0} = \log \frac{R_2 - (x-c)}{R_1 - (x+c)}, \ B_{1,1} = R_2 - R_1 + xB_{1,0},$$

(17.2)

$$B_{3,0} = \frac{1}{r^2}\left(\frac{x+c}{R_1} - \frac{x-c}{R_2}\right), \ B_{3,1} = \left(\frac{1}{R_1} - \frac{1}{R_2}\right) + xB_{3,0},$$

(17.3)

$$B_{m,n}(\mathbf{x}) = \int_{-c}^{c} \frac{\zeta^n}{|x-\zeta|^m} d\zeta \ (n = 0,1,2,...; m = -1,1,3,5,...) \ .$$

(17.4)

On the spheroid surface,

$$\frac{x^2}{a^2} + \frac{r^2}{b^2} = 1 \ (r^2 = y^2 + z^2, a \geq b),$$

(18.1)

$$r^2 = (1-e^2)(a^2 - x^2), \ R_1 = a + ex, \ R_2 = a - ex,$$

(18.2)

$$B_{1,0} = \log\frac{1+e}{1-e}, \ B_{3,0} = \frac{2e}{(1-e^2)(a^2 - e^2 x^2)},$$

(18.3)

where $e = c/a = \sqrt{a^2 - b^2}/a$

Then the surface velocity becomes

$$\mathbf{u}_0 = \left[U_1 + \frac{2\alpha_1}{e} - 2(\alpha_1 + \beta_1)\log\frac{1+e}{1-e}\right]\mathbf{e}_x - \frac{2}{e}\left(\alpha_1 - \frac{2e^2\beta_1}{1-e^2}\right)\frac{b^2\mathbf{e}_x + e^2 xr\mathbf{e}_r}{a^2 - e^2 x^2}$$
$$+ \left[U_2 - \frac{2e\beta_2}{1-e^2} - (\alpha_2 - \beta_2)\log\frac{1+e}{1-e}\right]\mathbf{e}_y - 2e\left(\alpha_2 - \frac{2e^2\beta_2}{1-e^2}\right)y\frac{b^2 x\mathbf{e}_x + a^2 r\mathbf{e}_r}{b^2(a^2 - e^2 x^2)}$$

(19)

To set $\mathbf{u}_0 = 0$, four equations for $\alpha_1, \alpha_2, \beta_1$ and β_2 can be obtained and lead to

solutions:

$$\alpha_1 = \frac{U_1 e^2}{-2e + (1+e^2)\log\dfrac{1+e}{1-e}} ; \ \alpha_2 = \frac{2U_2 e^2}{2e + (3e^2 - 1)\log\dfrac{1+e}{1-e}},$$

(20.1)

$$\beta_1 = \frac{1-e^2}{2e^2}\alpha_1 \; ; \; \beta_2 = \frac{1-e^2}{2e^2}\alpha_2 .$$

(20.2)

The force on the speroid is

$$\mathbf{F} = \int_{S\_spheroid}(p\mathbf{n}-\vec{\tau})dS = \int_{V\_spheroid}(\nabla P_s - \mu\nabla^2 U_S)dV = 8\pi\mu\vec{\alpha}$$

$$= -8\pi\mu\int_{-c}^{c}(-\alpha_1\mathbf{e}_x - \alpha_2\mathbf{e}_y)dx = 8\pi\mu a[U_1 C_{F1}\mathbf{e}_x + U_2 C_{F2}\mathbf{e}_y]$$

(21)

where

$$C_{F1} = \frac{8}{3}\frac{c\alpha_1}{aU_1} = \frac{8}{3}e^3[-2e+(1+e^2)\log\frac{1+e}{1-e}]^{-1}$$

(22.1)

$$C_{F2} = \frac{8}{3}\frac{c\alpha_2}{aU_2} = \frac{16}{3}e^3[2e+(3e^2-1)\log\frac{1+e}{1-e}]^{-1} .$$

(22.2)

For the uniform flow past a prolate sphere, $\mathbf{u} = U\mathbf{e}_y$

$$\mathbf{D} = -8\pi\mu U\int_{-c}^{c}\alpha_0\left[1+e\alpha_0 R_a + O(R_a^2)\right]d\xi ,$$

(23)

where $\alpha_0 = \dfrac{2e^2}{2e+(3e^2-1)\log\dfrac{1+e}{1-e}}$.

$$\rightarrow \mathbf{D} = 8\pi\mu U \frac{2e^2\times 2c}{2e+(3e^2-1)\log\dfrac{1+e}{1-e}}\left[1+\frac{2e^3 R_a}{2e+(3e^2-1)\log\dfrac{1+e}{1-e}}+O(R_a^2)\right]$$

$$= \frac{32\pi\mu Uae^3}{2e+(3e^2-1)\log\dfrac{1+e}{1-e}}\left[1+\frac{2e^3 R_a}{2e+(3e^2-1)\log\dfrac{1+e}{1-e}}+O(R_a^2)\right]$$

(24)